SAFETY LIMITS & RAPID SCANNING METHODS IN MAGNETIC PARTICLE IMAGING

A THESIS SUBMITTED TO
THE GRADUATE SCHOOL OF ENGINEERING AND SCIENCE
OF BILKENT UNIVERSITY
IN PARTIAL FULFILLMENT OF THE REQUIREMENTS FOR
THE DEGREE OF
MASTER OF SCIENCE
IN
ELECTRICAL AND ELECTRONICS ENGINEERING

By
Ömer Burak Demirel
July 2017

SAFETY LIMITS & RAPID SCANNING METHODS IN MAGNETIC PARTICLE IMAGING
By Ömer Burak Demirel
July 2017

We certify that we have read this thesis and that in our opinion it is fully adequate, in scope and in quality, as a thesis for the degree of Master of Science.

Emine Ülkü Sarıtaş Çukur (Advisor)

Ergin Atalar

Behçet Murat Eyüboğlu

Approved for the Graduate School of Engineering and Science:

Ezhan Karaşan
Director of the Graduate School

ABSTRACT

SAFETY LIMITS & RAPID SCANNING METHODS IN MAGNETIC PARTICLE IMAGING

Ömer Burak Demirel
M.S. in Electrical and Electronics Engineering
Advisor: Emine Ülkü Sarıtaş Çukur
July 2017

Magnetic Particle Imaging (MPI) is a new imaging modality that utilizes nonlinear magnetization of superparamagnetic tracers, with high sensitivity and zero-ionizing radiation advantages. Since the introduction of MPI in 2005, there have been substantial contributions to pre-clinical applications such as cancer imaging, cell tracking, and angiography. These studies have promising implications for future clinical human-sized MPI systems. However, the time-varying magnetic fields that are used during image acquisition are subject to human safety concerns, especially in applications that require rapid imaging. By forming electric field patterns in the body, these fields may result in peripheral nerve stimulation, also known as magnetostimulation. To prevent potential stimulations; the effects of frequency, duration, and direction of the fields, as well as body part size were previously investigated. This thesis investigates the effects of duty cycle and fat/water tissue ratio on magnetostimulation thresholds for the drive field in MPI. Human subject experiments with in-house magnetostimulation setup were conducted at 25 kHz, followed by anatomical Magnetic Resonance Imaging (MRI) of the subjects. Accordingly, magnetostimulation thresholds first decrease then increase with increasing duty cycle and reach a maximum at 100% duty cycle. The results also show that the thresholds are strongly correlated with fat/water tissue ratio. Finally, this thesis also demonstrates that MPI image quality can be preserved for rapid scanning scenarios within the human safety limits.

Keywords: magnetic particle imaging, magnetostimulation threshold, peripheral nerve stimulation, rapid imaging.

ÖZET

MANYETİK PARÇACIK GÖRÜNTÜLEME'DE GÜVENLİK SINIRLAMALARI & HIZLI TARAMA YÖNTEMLERİ

Ömer Burak Demirel
Elektrik ve Elektronik Mühendisliği, Yüksek Lisans
Tez Danışmanı: Emine Ülkü Sarıtaş Çukur
Temmuz 2017

Manyetik Parçacık Görüntüleme (MPG), süperparamanyetik parçacıkların lineer olmayan mıknatıslanmasını yüksek hassasiyet ve sıfır iyonize radyasyon avantajları ile kullanan yeni bir görüntüleme yöntemidir. MPG'nin 2005 yılında kullanıma sunulmasından bu yana, kanser görüntüleme, hücre takibi ve anjiyografi gibi klinik öncesi uygulamalara önemli katkılar sağlanmıştır. Bu çalışmalar insanlar için planlanan MPG sistemlerine yönelik umut verici etkilere sahiptir. Bununla birlikte, görüntüleme sırasında kullanılan zamanla değişen manyetik alanlar, özellikle hızlı görüntülemeyi gerektiren uygulamalarda insan güvenliği ile ilgili sınırlara uymalıdır. Vücutta elektrik alan örüntüleri oluşturan bu alanlar, manyetik uyarım olarak da bilinen periferik sinir uyarımına neden olabilirler. Oluşabilecek uyarımları önlemek amacıyla; manyetik alanın frekansı, atım süresi ve yönünün etkileri ile manyetik alan uygulanan vücut parçası boyutunun etkileri daha önce araştırılmıştır. Bu tez, görev döngüsü ve yağ/su doku oranının, MPG'de kullanılan eksitasyon alanları için manyetik uyarım eşikleri üzerine etkilerini araştırmaktadır. Özel yapım manyetik uyarım düzeneği ile insan deneyleri, 25 kHz'de gerçekleştirilmiştir ve ardından deneklerin anatomik yapıları Manyetik Rezonans Görüntüleme (MRG) ile görüntülenmiştir. Bu doğrultuda, manyetik uyarım eşiklerinin görev döngüsü arttıkça önce azaldığı, daha sonra artarak %100 görev döngüsünde maksimuma ulaştığı gözlenmiştir. Deney sonuçları ayrıca eşiklerin yağ/su doku oranı ile kuvvetli bir şekilde ilişkili olduğunu da göstermektedir. Bu tez son olarak, insan güvenliği sınırlarında kalan hızlı taramalar için MPG görüntü kalitesinin korunabildiğini göstermektedir.

Anahtar sözcükler: hızlı görütüleme,manyetik parçacık görütüleme, manyetik uyarım sınırları, periferik sinir uyarımı.

Acknowledgement

First of all, I would like to thank to my supervisor, Asst. Prof. Emine Ülkü Sarıtaş Çukur. I count myself very lucky to be one of her students. Additionally, I want to express my sincere gratitude for her great advices, excellence guidance and support during my thesis work.

I would also like to thank Prof. Dr. Ergin Atalar and Prof. Dr. Behçet Murat Eyüboğlu for their valuable feedbacks and being a member of my thesis committee.

I would like to thank the following funding agencies for supporting the work in this thesis: the Scientific and Technological Research Council of Turkey through TUBITAK Grant No 114E167 and 215E198, the European Commission through FP7 Marie Curie Career Integration Grant (PCIG13-GA-2013-618834), the Turkish Academy of Sciences through TUBA-GEBIP 2015 program, and the BAGEP Award of the Science Academy.

I would also like to thank their motivation and support of my closest friends, Onur Tan, Batıkan Türkmen, İlker Burak Kurt, Mustafa Eflatun, Cem Sevim, Egehan Eğitim, Nurullah Karakoç, Efe Yavuzer and Batuhan Yıldız. I also would like to thank my roommate Oğuz Kaan Karakoyun for his great support.

Next comes, National Magnetic Resonance Research Center (UMRAM) people who were very kind and supportive during my thesis work. I want to thank Mustafa Can Delikanlı for his support with hardware works and helpings during MRI scans. I also would like to thank our laboratory members, Mustafa Ütkür, Yavuz Muslu, Ali Alper Özaslan, Toygan Kılıç, Sevgi Gökçe Kafalı and Akbar Alipour for being such a family in this short time.

Last but not least, I want to thank my beloved family, my father Bülent Mecit Demirel for his endless support and trust on my education, my mother Ayfer Postoğlu for her undying love and eternal trust on me, my brothers Emre Demirel and Alp Demirel for their supports.

Contents

List of Figures

List of Tables

Chapter 1

Introduction

Magnetic Particle Imaging (MPI) distinguishes spatial distribution of superparamagnetic iron oxide nanoparticles (SPIOs) by using their nonlinear magnetization [1, 2]. In MPI, permanent or super-conductive magnets are placed to create a region called the field-free-point (FFP), where there is no magnetic field. Additionally, time-varying magnetic fields called drive fields are applied to create a magnetization response from the SPIOs in the FFP. Through spatial scanning of the FFP by using focus fields or mechanical movement, MPI generates an image of the 3D spatial distribution of SPIOs [1, 3]. MPI has a wide range of potential imaging applications such as cancer imaging [4], stem-cell tracking [5, 6], angiography [7, 8], temperature mapping [9], hyperthermia [10], multi-color imaging [11, 12], and functional imaging [13]. These applications are being developed by using MPIs high contrast, high sensitivity, and rapid imaging capabilities.

Time-varying magnetic fields that leverage the non-linear magnetization of SPIOs are subject to human safety limits in two different ways: peripheral nerve stimulation (PNS), also known as magnetostimulation, and specific absorption rate (SAR) [14, 15, 16]. From these two concerns, SAR limits were vastly investigated in magnetic resonance imaging (MRI) for the radio frequency (RF) magnetic fields, that typically operate at 64 MHz or 128 MHz [16]. PNS limits

were also widely investigated for the gradient magnetic fields in MRI that operate around 1 kHz switching rates [17, 18]. Safety limits of time-varying magnetic fields in MPI, on the other hand, has been a subject of study only recently. The drive field frequency dependence of the thresholds for frequencies up to 150 kHz [19, 20, 21] was investigated, showing that thresholds decrease with increasing frequency [19]. Accordingly, for the human torso, the stimulation limits are expected to be around 7 mT when operating at or beyond 25 kHz [19]. Furthermore, it was shown that the magnetostimulation thresholds also depend on the direction of the drive field [20, 21, 22], and that they decrease with increasing pulse duration and stabilize for pulses longer than approximately 20 ms [23].

To avoid potential safety hazards and to optimize the imaging parameters in MPI, the factors that affect magnetostimulation need to be further investigated. One factor of interest is the duty cycle of the applied field drive field. Unlike the gradient fields in MPI that are pulsed, the drive field in MPI is typically applied continuously, with full duty cycle. Hence, whether using the magnetic field at such high duty cycles have any adverse affects on imaging speed was investigated in this thesis. For this purpose, magnetostimulation experiments on the human arm were conducted at different duty cycles. In addition, these experiments revealed an interesting observation: subjects with similar arm sizes sometimes had significantly different magnetostimulation thresholds, and this disparity seemed to be related to the muscularity of the arms. However, a previous study that looked at the correlations between anatomical measurements and PNS found no significant correlation between any measured physiologic parameters such as body fat percentage and PNS thresholds [24]. These experiments were performed on the human torso. In contrast, recent studies on magnetostimulation limits revealed that magnetostimulation thresholds actually depend on anatomical measures: via experiments performed on both the arms and legs of human subjects, a strong correlation between the inverse of body part size and magnetostimulation thresholds was shown [19]. With this motivation, this thesis also investigates the effects of fat/muscle ratio on magnetostimulation thresholds via experiments on the human arm.

In addition to drive fields in MPI, focus fields are utilized to shift the FFP

across a wider region of interest. Conventionally, piecewise constant focus fields were used in MPI to cover a wide field-of-view (FOV) by dividing it into smaller overlapping pieces, also known as partial field-of-views (pFOVs) [3, 8]. The step-by-step coverage of the FOV is an unnecessarily time-consuming approach, and more rapid scans can be developed to reduce scan times. Therefore, recent works utilized a linearly ramping focus field approach [25, 26], where the images were reconstructed using x-space MPI reconstruction. In practice, these focus fields operate at switching rates that are close to or slower than the gradient magnetic fields in MRI. In MRI, there are officially recommended slew rates for the operation of gradient magnetic fields in rapid scanning techniques. A maximum slew rate of 20 T/s should not be exceeded for axial gradients according to regulations set by USA/FDA (1989), Japan (1991), and Germany/BFS (1995) [17]. It is assumed that the focus fields in MPI also need to abide by 20 T/s maximum slew rates. Rapid scanning techniques have previously been proposed for an alternative image reconstruction technique called system-matrix reconstruction, where the effects of rapid scanning on image quality were investigated [27]. However, the effects of rapid scanning on image quality have not yet been investigated for x-space MPI image reconstruction.

In this thesis, I first present the effects of duty cycle on magnetostimulation thresholds via human-subject experiments on the arm. The results show that the thresholds first decrease and then increase with increasing duty cycle. Importantly, the thresholds reach a maximum at 100% duty cycle, which is a promising finding for fast scanning techniques that rely on full-duty-cycle imaging. I also demonstrate for the first time that there is a high linearity between the ratio of fat/water tissues and magnetostimulation thresholds. The experimental results also show that the magnetostimulation thresholds are highly correlated with the effective radius of the core muscle content (i.e., excluding the surrounding fat). Finally, I demonstrate via simulations that the image quality in x-space MPI can be preserved when focus field slew rates are kept within the human safety limits. These findings will help in determining the optimum imaging parameters for future clinical applications of MPI.

Chapter 2

Magnetic Particle Imaging (MPI) Background

2.1 X-Space MPI Theory

2.1.1 1-D X-Space MPI Signal & Image Equations

In Magnetic Particle Imaging (MPI), the signal induced in the receiver coils originates from the magnetization response of superparamagnetic iron oxide nanoparticles (SPIOs) that are in the field free point (FFP). Particles in/near the FFP can response to the applied time-varying drive fields, whereas particles outside the FFP can not produce any magnetization due to their saturation. A schematic of an MPI scanner is presented in Fig. 2.1. As shown in this figure, two electromagnets of permanent magnets with opposing magnetic fields create a FFP at the center of the scanner. The static magnetic field that generates this FFP is called the selection field.

The magnetization response of SPIOs is well defined with Langevin physics [3]. The SPIOs try to align their magnetic moments to the applied time-varying magnetic fields (i.e., drive fields). This Langevin response is mathematically

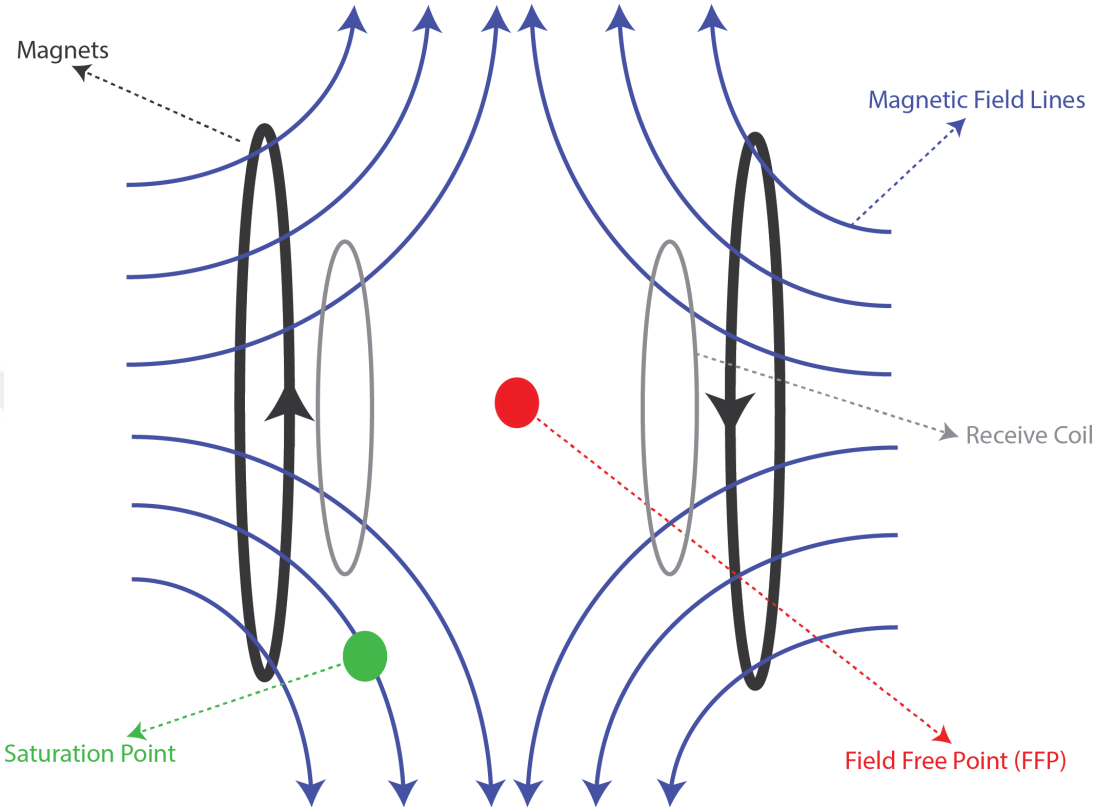

Figure 2.1: Schematic of an MPI scanner with a 2D representation of magnetic fields (blue lines). Currents flow in opposite directions to create a field free point (FFP) at the center of the scanner. The red dot represents the FFP where the SPIOs are not saturated and applied time-varying drive fields can elicit their non-linear magnetization response. This magnetization response can be picked up by inductive receive coils (indicated with gray loops). The green dot represents the point where the static magnetic fields is relatively large, so that the SPIOs are saturated.

represented in Eq. 2.1 and is plotted in Fig. 2.2.a where $\frac{H}{H_{sat}}$ is a dimensionless constant [3].

$$\begin{aligned} M(H) &= Nm\mathcal{L}(\frac{H}{H_{sat}}) \\ &= Nm(coth(\frac{H}{H_{sat}}) - \frac{H_{sat}}{H}) \end{aligned} \tag{2.1}$$

where $\mathcal{L}(\cdot)$ is the Langevin function and

$$H_{sat} = \frac{1}{k} = \frac{k_B T}{\mu_0 m} \tag{2.2}$$

and H is the applied external magnetic field [A/m], N [nanoparticles/m^3], k_B is Boltzmann constant [JK^{-1}], T is temperature [K], μ_0 is vacuum permeability [Tm/A], $m = M_{sat}\pi d^3/6$ and $M_{sat} \approx 0.6T/\mu_0$ and H_{sat} has units of [A/m].

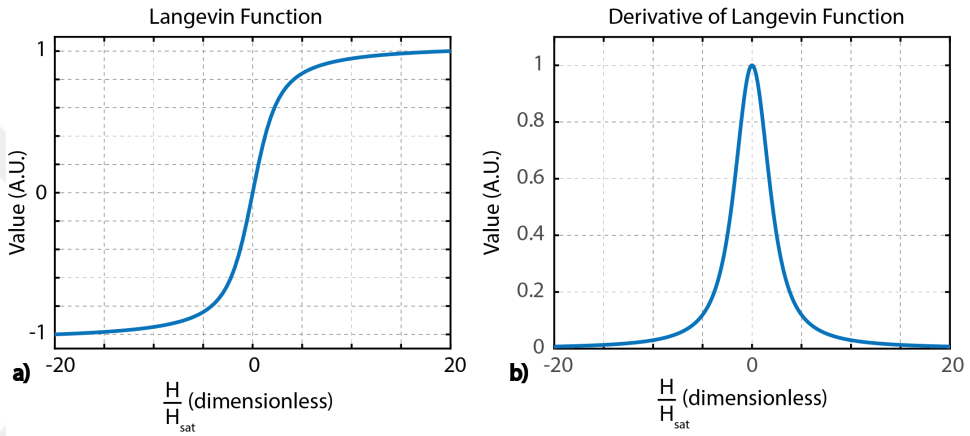

Figure 2.2: a) The Langevin Function ($\mathcal{L}$) with respect to $\frac{H}{H_{sat}}$,which is a dimensionless constant. b) Derivative of the Langevin Function ($\dot{\mathcal{L}}$) with respect to $\frac{H}{H_{sat}}$.

The derivative of the Langevin function is mathematically given in Eq. 2.3 and is illustrated in Fig. 2.2.b [3].

$$\dot{\mathcal{L}}\left[\frac{H}{H_{sat}}\right] = Nm\left(\frac{1}{(\frac{H}{H_{sat}})^2} - \frac{1}{sinh^2(\frac{H}{H_{sat}})}\right) \tag{2.3}$$

In Fig. 2.3, the red signal represents the signal induced in the receive coils when SPIOs are located at the FFP and the drive fields are applied. Only the SPIOs that are in/near the FFP can respond to the drive fields. However, SPIOs that are not in the FFP region will not produce any signal even though drive fields are applied. In Fig. 2.3, the green signal represents that there is no signal induced in the receive coils when the SPIOs are saturated.

It is typically assumed that the selection field generates a static linear gradient field, G [A/m/m]. A time-varying field H_0 [A/m] as the drive field is then applied,

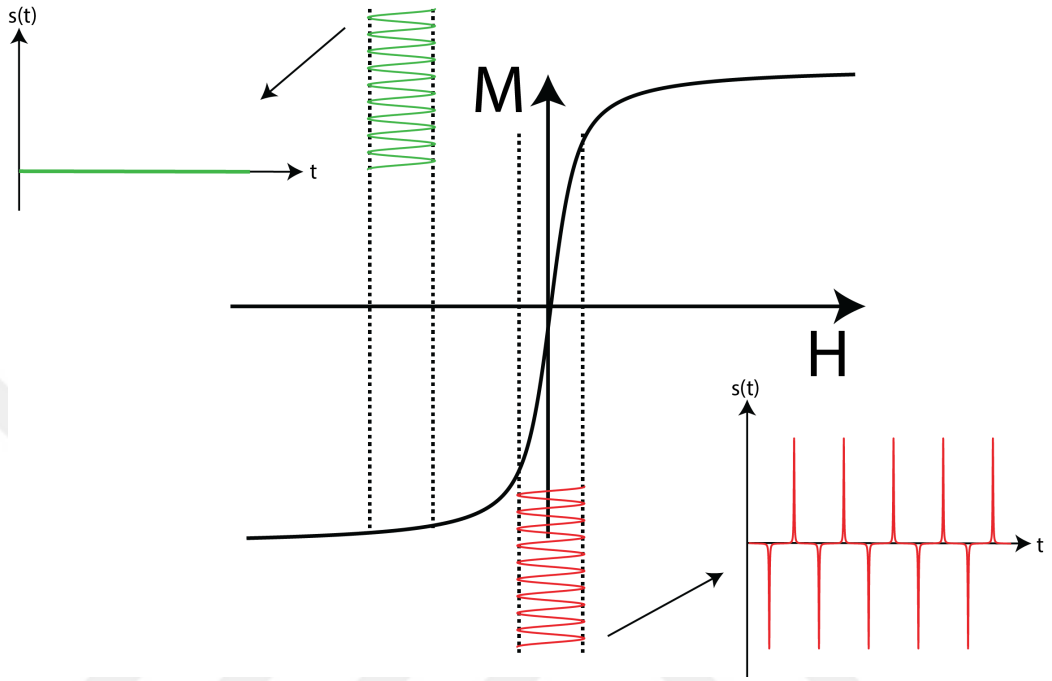

Figure 2.3: The signal induced in the receive coils from the SPIOs is illustrated with the red signal. SPIOs that are located in/near the FFP can produce magnetization under applied magnetic fields. SPIOs are saturated when they are not in the FFP and the drive fields can not alter their magnetization sufficiently. The green signal illustrates that the saturated SPIOs do not generate any signal in MPI.

so that the total magnetic field at position x can be represented as follows [3]:

$$H(x,t) = H_0(t) - Gx \tag{2.4}$$

When we equalize Eq. 2.4 to zero, we can find the instantaneous location of the FFP [3]:

$$x_s(t) = G^{-1}H_0(t) \tag{2.5}$$

We can use the exact location of FFP and write the following formula [3]:

$$H(x,t) = Gx_s(t) - Gx = G(x_s(t) - x) \tag{2.6}$$

If we use the information from Eq. 2.1, we can write the magnetization of

SPIOs as follows [3]:

$$M(H) = m\rho\mathcal{L}(\frac{H}{H_{sat}}) \tag{2.7}$$

where m [Am^2] represents the magnetic moment, ρ [nanoparticle/m^3] represents nanoparticle density. If we assume that there is nanoparticle distribution along only one axis (x axis in this scenario), nanoparticle distribution can be expressed as follows [3]:

$$\rho(x, y, z) = \rho(x)\delta(y)\delta(z) \tag{2.8}$$

and magnetization of SPIOs become [3]:

$$M(H) = m\rho(x)\delta(y)\delta(z)\mathcal{L}\left(\frac{H}{H_{sat}}\right) \tag{2.9}$$

Then, we can re-write the magnetization by using Eq. 2.6 as follows [3]:

$$M(x, t) = m\rho(x)\delta(y)\delta(z)\mathcal{L}\left(\frac{G(x_s(t) - x)}{H_{sat}}\right) \tag{2.10}$$

Eq. 2.10 gives us the magnetization of SPIOs when FFP is at position $x_s(t)$. In order to write the signal equation in MPI, we need to find the flux Φ due to all SPIOs in the volume [3]:

$$\begin{aligned}\Phi(t) &= -m\int\int\int \rho(u)\delta(v)\delta(w)\mathcal{L}\left[\frac{G(x_s(t) - u)}{H_{sat}}\right]dudvdw \\ &= -m\int \rho(u)\mathcal{L}\left[\frac{G(x_s(t) - u)}{H_{sat}}\right]du \\ &= -m\rho(x) * \mathcal{L}\left[\frac{Gx}{H_{sat}}\right]\Bigg|_{x=x_s(t)}\end{aligned} \tag{2.11}$$

Eq. 2.11 shows that the flux is the convolution of the Langevin function with the nanoparticle density. The inductive receive coils with $-B_1$ [T/A] sensitivity senses the time derivative of this flux. Therefore, the signal equation of 1-D MPI becomes in volts [V] [3]:

$$s(t) = B_1 \frac{d\Phi}{dt} = B_1 m \rho(x) * \dot{\mathcal{L}}\left[\frac{Gx}{H_{sat}}\right]\Big|_{x=x_s(t)} \frac{G\dot{x}_s(t)}{H_{sat}} \tag{2.12}$$

Finally, image equation is defined as the signal divided by the derivative of $x_s(t)$ and extra terms [3].

$$IMG(x_s(t)) = \frac{s(t)}{B_1 m \frac{G\dot{x}_s(t)}{H_{sat}}} \tag{2.13}$$

This equation represents a convolution of magnetic particle density with the imaging point spread function (PSF) [3].

$$IMG(x_s(t)) = \rho(x) * \dot{\mathcal{L}}\left[\frac{Gx}{H_{sat}}\right]\Big|_{x=x_s(t)} \tag{2.14}$$

In Eq. 2.14, the 1-D PSF is represented by the derivate of the Langevin function which can be seen in Eq. 2.3 and Fig. 2.2.b.

2.1.2 Multidimensional X-Space MPI Signal & Image Equations

To extend the 1-D formulation of MPI into multi-dimensional signal and image equation, following definitions are presented [28]:

$$\mathbf{x} = \begin{bmatrix} x \\ y \\ z \end{bmatrix} \tag{2.15}$$

where $\mathbf{x}$ denotes the position in real space. For an ideal MPI system, $\mathbf{G}$ denotes the gradient matrix as follows (see A.1 for the gradient matrix in details) [28]:

$$G = G_{zz} \begin{bmatrix} -\frac{1}{2} & 0 & 0 \\ 0 & -\frac{1}{2} & 0 \\ 0 & 0 & 1 \end{bmatrix} \tag{2.16}$$

Next, the homogeneous time-varying magnetic fields (i.e., drive fields) are defined as [28]:

$$H_s(t) = \begin{bmatrix} H_x(t) \\ H_y(t) \\ H_z(t) \end{bmatrix} \tag{2.17}$$

By using the gradient matrix from Eq. 2.16 and drive fields from Eq. 2.17, total magnetic field can be written as [28]:

$$\begin{aligned} H(x,t) &= H_s(t) - Gx \\ &= H_s(t) - G_{zz} \begin{bmatrix} -\frac{1}{2} & 0 & 0 \\ 0 & -\frac{1}{2} & 0 \\ 0 & 0 & 1 \end{bmatrix} \begin{bmatrix} x \\ y \\ z \end{bmatrix} \end{aligned} \tag{2.18}$$

To solve for the instantaneous position of the FFP, we need to equalize $H(x,t)$ to zero and obtain the following [28]:

$$x_s(t) = G^{-1} H_s(t) \tag{2.19}$$

Therefore, magnetic field at an arbitrary position ($\mathbf{x}$) can be found as [28]:

$$H(x,t) = G(x_s(t) - x) \tag{2.20}$$

The magnetization of the SPIOs are defined in Eq. 2.1. The same formulation is preserved with in multi-dimensional extension [28]:

$$M(H) = \rho m \mathcal{L}\left[\frac{\|H\|}{H_{sat}}\right] \hat{H} \tag{2.21}$$

where $\hat{H} = H/\|H\|$. If we have a magnetic particle density $\rho(x)$, we can write the magnetic density equation with respect to the instantaneous location of the FFP [28]:

$$M(x,t) = \rho(x) m \mathcal{L}\left[\frac{\|G(x_s(t)-x)\|}{H_{sat}}\right] \times \frac{G(x_s(t)-x)}{\|G(x_s(t)-x)\|} \tag{2.22}$$

Therefore, magnetic moment of the SPIOS can be written in the form of:

$$m(t) = \int\int\int \rho(u) m \mathcal{L}\left[\frac{\|G(x_s(t)-u)\|}{H_{sat}}\right] \times \frac{G(x_s(t)-u)}{\|G(x_s(t)-u)\|} du \tag{2.23}$$

Integrating Eq. 2.23 over the imaging volume results in a 3-dimensional convolution of the Langevin function with the nanoparticle distribution [28]:

$$m(t) = m\rho(x) * * * \mathcal{L}\left[\frac{\|Gx\|}{H_{sat}}\right] \frac{Gx}{\|Gx\|}\Bigg|_{x=x_s(t)} \tag{2.24}$$

The total magnetization from SPIOs induce a signal in the receiver coil with $-B_1$ (T/A) sensitivity, which yields the following multi-dimensional signal equation [28]:

$$s(t) = \frac{d}{dt}\int\int\int B_1(u) M(u,t) du \tag{2.25}$$

In order to solve the signal equation some derivations are needed. First of all, following four definitions are presented (derivations can be found in A.2 and A.3) [28]:

$$r \triangleq \frac{G(x_s(t)-x)}{H_{sat}} \tag{2.26}$$

$$\dot{r} = \frac{G\dot{x}_s(t)}{H_{sat}} \tag{2.27}$$

$$\hat{r} \triangleq \frac{r}{\|r\|} \tag{2.28}$$

$$\dot{\hat{r}} = \frac{\dot{r}}{\|r\|} + \frac{\dot{r}^T r}{\|r\|^3} r \tag{2.29}$$

We also need to decompose $\dot{r}$ into its tangential and normal parts [28]:

$$\dot{r} = \dot{r}_{\|} + \dot{r}_{\perp} \tag{2.30}$$

where

$$\dot{r}_{\|} = (\dot{r}.\hat{r})\hat{r} = \left(\dot{r} \cdot \frac{r}{\|r\|}\right)\hat{r} \tag{2.31}$$

$$\dot{r}_{\perp} = \left[\dot{r} - \left(\dot{r} \cdot \frac{r}{\|r\|}\right)\hat{r}\right] \tag{2.32}$$

Moreover, we define the Langevin function and its derivative for multi-dimensional expressions (mathematical derivation of the Eq. 2.33 is shown in A.4 to A.7) [28]:

$$\frac{d}{dt}\mathcal{L}(\|r\|)\hat{r} = \dot{\mathcal{L}}(\|r\|)\dot{r_{\|}} + \frac{\mathcal{L}(\|r\|)}{\|r\|}\dot{r_{\perp}} \tag{2.33}$$

Now, we are ready to write the multi-dimensional MPI signal formulation as follows [28]:

$$\begin{aligned} s(t) &= \frac{d}{dt}\int\int\int B_1(u) m\rho(u)\mathcal{L}(\|r\|)\hat{r}du \\ &= \int\int\int B_1(u) m\rho(u)\left[\dot{\mathcal{L}}(\|r\|)\dot{r_{\|}} + \frac{\mathcal{L}(\|r\|)}{\|r\|}\dot{r}_{\perp}\right]du \end{aligned} \tag{2.34}$$

However, Eq. 2.34 becomes complicated when we replace $r = \frac{G(x_s(t)-x)}{H_{sat}}$. Therefore, simplifications are needed to organize the signal equation. Those simplifications are presented in A.8 to A.10 [28]. To simplify the PSF, further simplifications are made on the equations, as given in A.11 to A.16 [28].

After all of the above definitions and derivations, we can finally write the following multi-dimensional MPI signal equation [28]:

$$s(t) = B_1(x)m\rho(x) * * * \frac{\|\dot{x}_s\|}{H_{sat}} h(x)\hat{\dot{x}}_s \Bigg|_{x=x_s(t)} \tag{2.35}$$

where $h(x)$ is the PSF:

$$h(x) = \dot{\mathcal{L}}\left(\frac{\|Gx\|}{H_{sat}}\right)\frac{Gx}{\|Gx\|}\left[\frac{Gx}{\|Gx\|}\right]^T G + \frac{\mathcal{L}\left(\frac{\|Gx\|}{H_{sat}}\right)}{\frac{\|Gx\|}{H_{sat}}}\left(I - \frac{Gx}{\|Gx\|}\left[\frac{Gx}{\|Gx\|}\right]^T\right)G \tag{2.36}$$

which consists of tangential and normal envelopes as follows (see in Fig. 2.4) [28]:

$$ENV_T = \dot{\mathcal{L}}\left(\frac{\|Gx\|}{H_{sat}}\right) \tag{2.37}$$

$$ENV_N = \frac{\mathcal{L}\left(\frac{\|Gx\|}{H_{sat}}\right)}{\frac{\|Gx\|}{H_{sat}}} \tag{2.38}$$

In addition to these, we have vector components of $h(x)$ and velocity vector $\hat{\dot{x}}_s$. If $\hat{\dot{x}}_s$ is aligned with x unit vector, then we have the following [28]:

$$if \quad \hat{\dot{x}}_s = \hat{e}_1 \tag{2.39}$$

$$then \quad h_{\|}(x) = \hat{e}_1 \cdot h(x)\hat{e}_1 \quad (collinear) \tag{2.40}$$

$$then \quad h_{\perp,1}(x) = \hat{e}_2 \cdot h(x)\hat{e}_1 \quad (transverse) \tag{2.41}$$

$$then \quad h_{\perp,2}(x) = \hat{e}_3 \cdot h(x)\hat{e}_1 \quad (transverse) \tag{2.42}$$

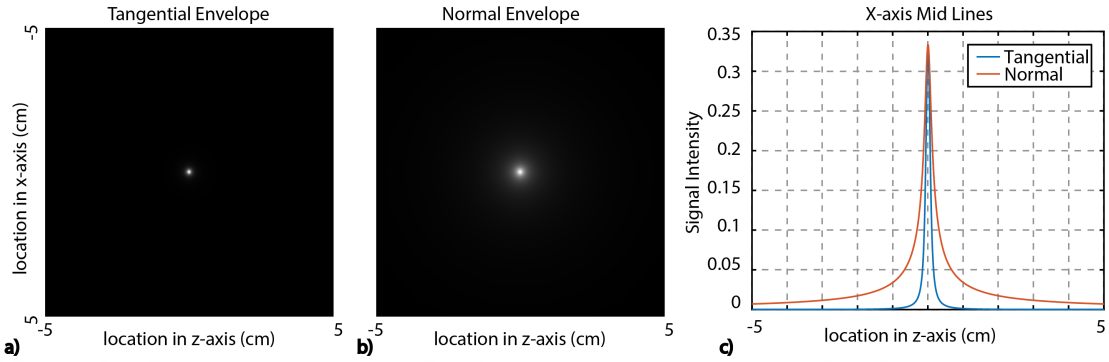

Figure 2.4: a) The tangential and b) the normal components of the PSF for $G_{xx} = 3\ T/m$ and $G_{zz} = 3\ T/m$. The tangential and normal envelopes represent the maximum attainable resolution in MPI. c) The x-axis mid-lines of the tangential and normal envelopes show that the tangential envelope is significantly narrower.

Then, we can express the collinear and transverse components of PSF as follows (derivation of the collinear and transverse components can be found A.17 to A.24) [28]:

$$h_{\parallel}(x,y,z) = \frac{\dot{\mathcal{L}}\left(\frac{H(x,y,z)}{H_{sat}}\right)}{H(x,y,z)^2} G_{zz}^3 z^2 + \frac{\mathcal{L}\left(\frac{H(x,y,z)}{H_{sat}}\right)}{\frac{H(x,y,z)}{H_{sat}}} G_{zz}\left(1 - \frac{G_{zz}^2 z^2}{H(x,y,z)^2}\right) \tag{2.43}$$

$$h_{\perp,1}(x,y,z) = \frac{\dot{\mathcal{L}}\left[\frac{H(x,y,z)}{H_{sat}}\right]}{H(x,y,z)^2} G_{xx} G_{zz}^2 xz - \frac{\mathcal{L}\frac{H(x,y,z)}{H_{sat}}}{\frac{H(x,y,z)}{H_{sat}}} \frac{G_{xx} G_{zz}^2 xz}{H(x,y,z)^2} \tag{2.44}$$

The collinear and transverse components of the PSF depends on the scanning direction ($\hat{x}_s$), as shown in Fig. 2.5. Note that, when scanning direction and receive coil are aligned, we obtained the collinear component of the PSF where scanning direction and receive coil are perpendicular we obtained the transverse component of PSF.

Now, we are ready for forming the reconstruction part by using the following definitions [28]:

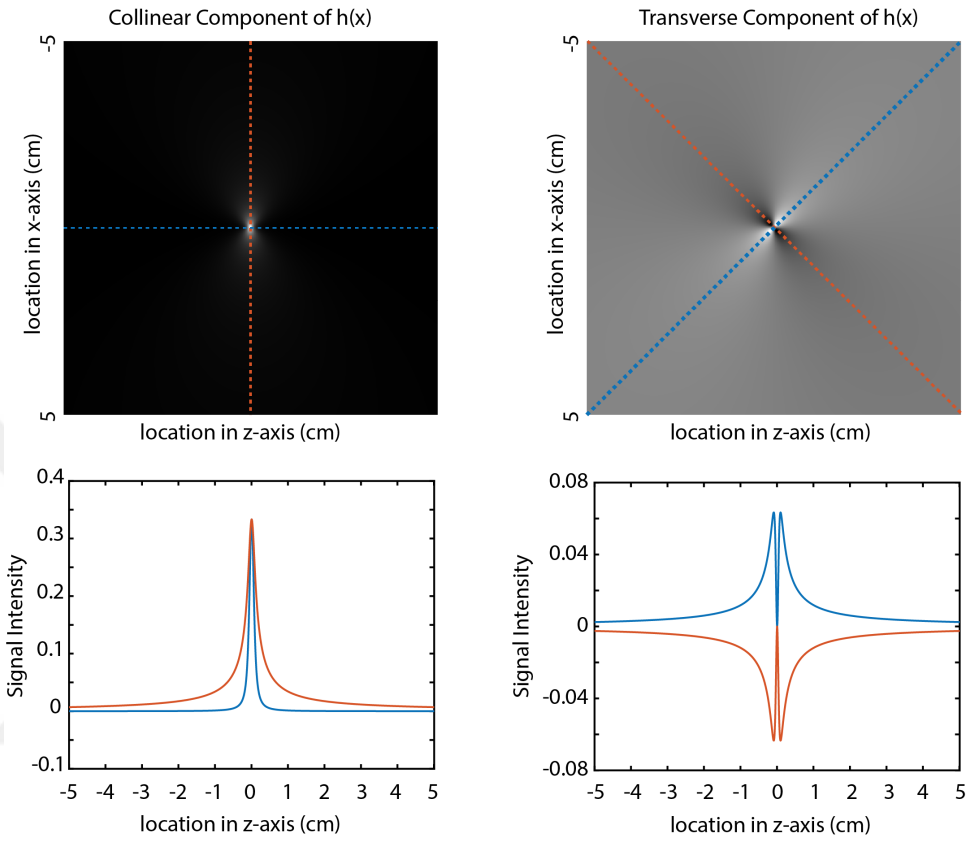

Figure 2.5: [Top] The collinear and transverse components of the PSF. [Bottom] Corresponding line segments for the collinear and transverse PSFs. These components depend on the scanning direction. If the scanning direction and receive coil are aligned then collinear component of the PSF is observed. If the scanning direction and receive coil are perpendicular then transverse component of the PSF is observed.

$$s_{\parallel}(t) = \hat{\dot{x}}_s \cdot s(t) \tag{2.45}$$

$$s_{\perp,1}(t) = (\hat{\dot{x}}_s \times \hat{e}_1) \cdot s(t) \tag{2.46}$$

$$s_{\perp,2}(t) = [(\hat{\dot{x}}_s \times \hat{e}_1) \times \hat{e}_2] \cdot s(t) \tag{2.47}$$

Finally, we can write the multi-dimensional image equation of the MPI system

as follows [28]:

$$\begin{aligned} IMG_{\|}(x_s(t)) &= \frac{s_{\|}(t)}{\|\dot{x}_s\|} \\ &= \rho(x) * * * \hat{\dot{x}}_s \cdot h(x)\hat{\dot{x}}_s \Big|_{x=x_s(t)} \end{aligned} \tag{2.48}$$

In Fig. 2.6, the images for the same phantom for the case of 3 different PSFs are presented.

2.2 Magnetostimulation Theory

Time-varying magnetic fields induce electric fields on the conductive tissue. These electric fields can cause peripheral nerve stimulation (PNS), also known as magnetostimulation. To formalize the magnetostimulation thresholds, the fundamental law of electro-stimulation can be used as follows [14]:

$$\frac{1}{\tau}\int^{\tau} E dt \geq E_{rheo}\left(1 + \frac{\tau_c}{\tau}\right) \tag{2.49}$$

where E_{rheo} represents the rheobase (minimum electric field amplitude) that can contract the muscles. For instance, myelinated fibers have a rheobase value around 6.2 [V/m] and typical cardiac muscle fibers have a rheobase value around 60 [V/m] [18]. On the other hand, τ_c represents the chronaxie time, which is the time constant for the depolarization time of nerves [29]. For example, the chronaxie time for the myelinated fibers are between 20 and 600 μsec, while that of the cardiac muscles are around 2 $msec$ [18]. In Fig. 2.7, we can see the relationship between the strength of the threshold electric field and the duration when $\tau_c = 0.1$ ms and $E_{rheo} = 6.2$ [V/m] to contract the muscles.

If we assume a magnetic field in x direction as follows [19]:

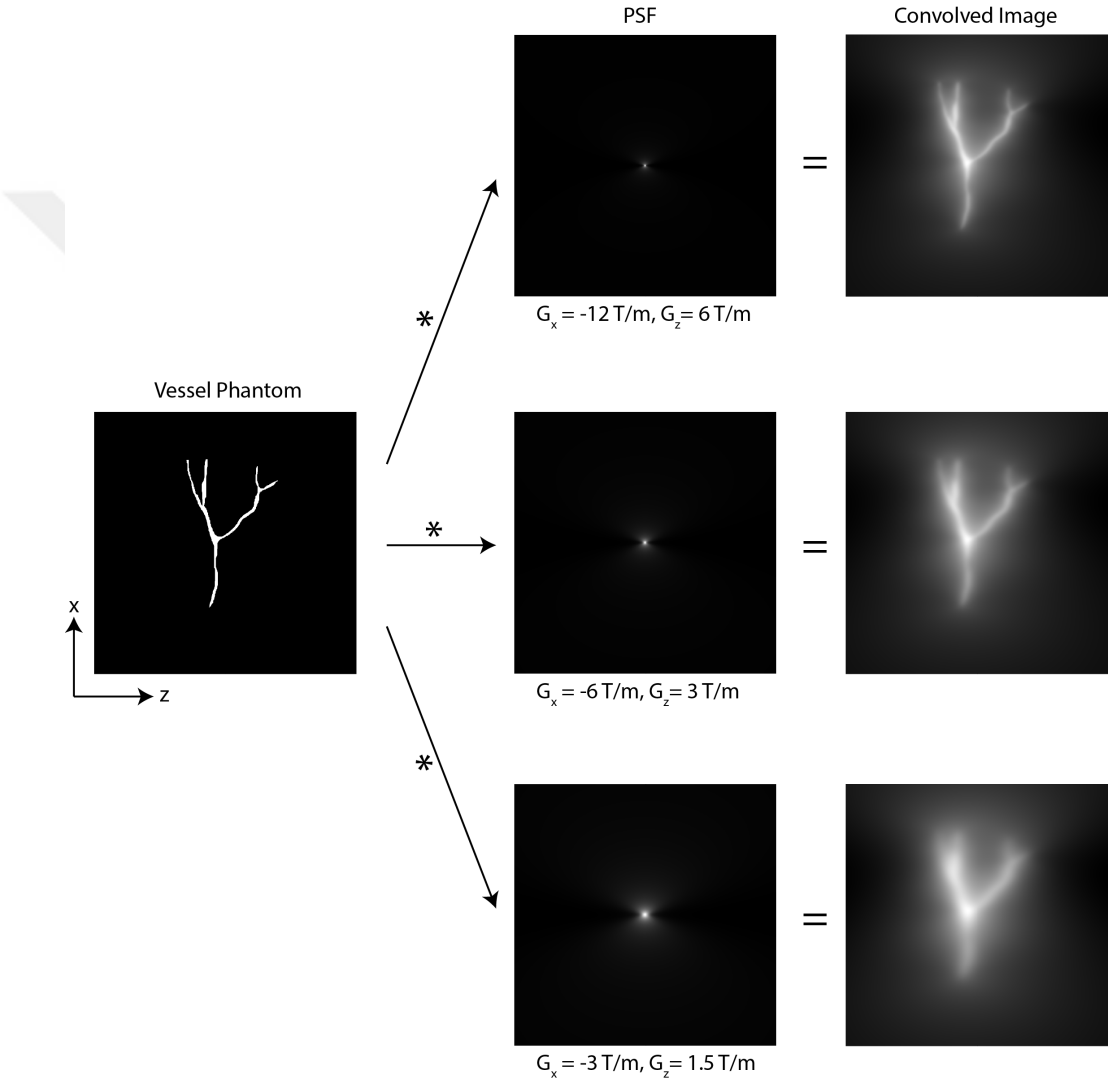

Figure 2.6: A vessel phantom and the imaging PSFs for 3 different gradients are shown. Corresponding convolved MPI images are shown in the rightmost column. Higher gradients result in narrower PSFs, and therefore higher resolution images. The upper left bifurcation of the vessel phantom is better resolved using higher gradients.

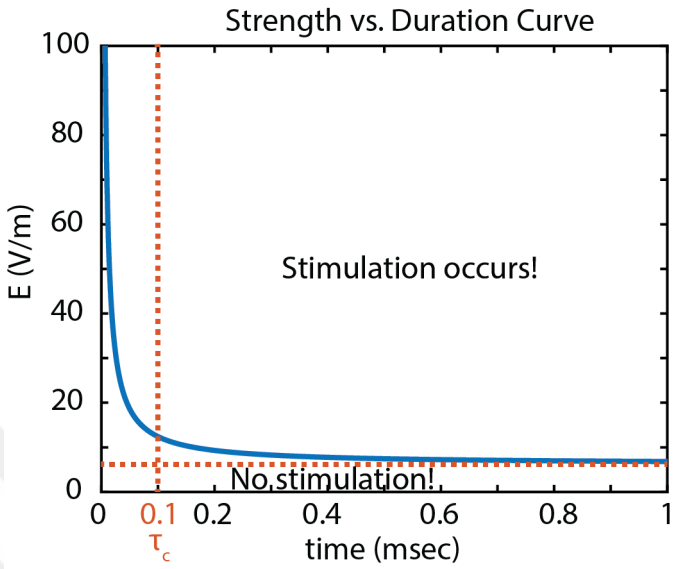

Figure 2.7: The threshold electric field amplitude vs. duration, plotted for muscle contraction with $\tau_c = 0.1$ ms and $E_{rheo} = 6.2$ [V/m].

$$B_x(t) = B_x sin(2\pi f_0 t) \tag{2.50}$$

and use the Faraday's law;

$$\oint Edl = \frac{d}{dt} \int \int Bds \tag{2.51}$$

we can obtain the following formula:

$$E = c.r \frac{dB}{dt} \tag{2.52}$$

where $c = 1/2$. However, the human body can be represented as a prolate spheroid (see Fig. 2.8). Hence, the c value will change according to the minor and major axis ratios, as well as the magnetic field orientation [18, 30].

Therefore, we can write the electric field as follows [19]:

$$E = r\pi f_0 B_x cos(2\pi f_0 t) \tag{2.53}$$

Now, we can use Eq. 2.49:

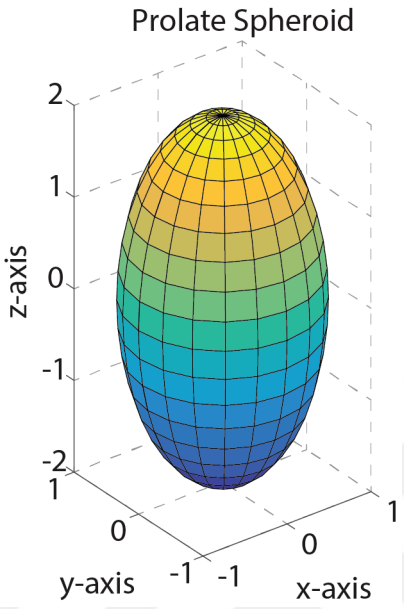

Figure 2.8: A prolate spheroid with the formulation $\frac{x^2+y^2}{a^2} + \frac{z^2}{b^2} = 1$, where $a = 1$ and $b = 2$.

$$\int^{\tau} Edt = \int^{\tau} c.r\frac{dB}{dt}dt = c.r\Delta B(\tau) \tag{2.54}$$

where $\Delta B(\tau)$ is the B-field excursion. If we combine Eq. 2.49 and Eq. 2.54, we can find the following equality [19]:

$$\begin{aligned} \frac{1}{\tau}\left[c.r\Delta B(\tau)\right] &\geq E_{rheo}\left(1+\frac{\tau_c}{\tau}\right) \\ \Delta B(\tau) &\geq \frac{E_{rheo}\tau_c}{c.r}\left(1+\frac{\tau}{\tau_c}\right) \\ and \quad define \quad \Delta B_{min} &= \frac{E_{rheo}\tau_c}{c.r} \\ \Delta B(\tau) &\geq \Delta B_{min}\left(1+\frac{\tau}{\tau_c}\right) \end{aligned} \tag{2.55}$$

We can further modify the formulation using the fact that the rise time for peak-to-peak amplitude of sinusoidal fields is equal to one half of the period [19]:

$$B_{pp} \geq \Delta B_{min} \left(1 + \frac{1}{2 f_0 \tau_c} \right) \tag{2.56}$$

Here, ΔB_{min} can be determined as the minimum peak-to-peak amplitude for high frequencies. In Fig. 2.9, normalized magnetostimulation threshold curve, $B_{pp}/\Delta B_{min}$, is plotted with respect to frequency for $\tau_c = 100\mu s$. This plot shows that magnetostimulation threshold converge to an asymptote at high frequencies.

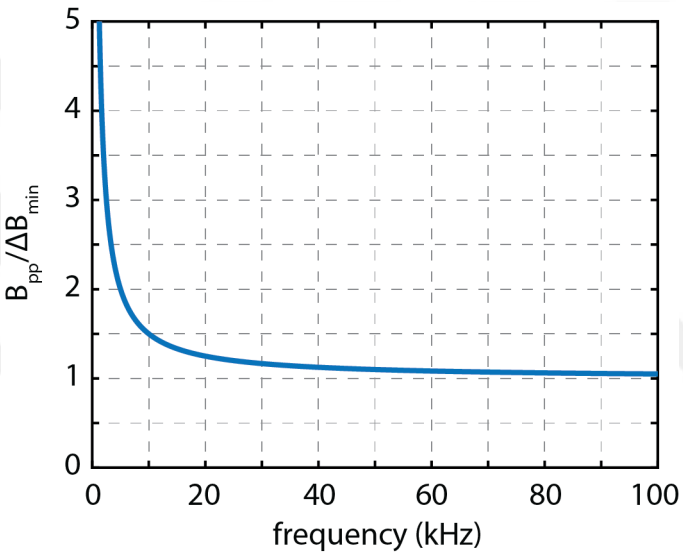

Figure 2.9: The normalized magnetotimulation threshold, $B_{pp}/\Delta B_{min}$, as a function of frequency for $\tau_c = 100\mu s$.

Chapter 3

Duty Cycle Effects on Magnetostimulation Thresholds

This chapter is based on the publication titled "Effects of Duty Cycle on Magnetostimulation Thresholds in MPI" O.B. Demirel, E.U. Saritas, International Journal on Magnetic Particle Imaging (2017). Reproduced with permission from Infinite Science Publishing, under a Creative Commons License.

3.1 Introduction

Time-varying magnetic fields are subject to human safety limits on magnetostimulation (also called peripheral nerve stimulation) and specific absorption rate (SAR) [14, 15, 16]. Of these two factors, SAR limits were widely investigated for the radiofrequency (RF) fields in MRI (e.g., at 64 MHz or 128 MHz) [16]. Likewise, the magnetostimulation limits of MRI gradient fields operating at lower frequencies of around 1 kHz were also investigated, with the goal of achieving high resolution and rapid imaging capabilities [17, 18]. Similarly, the safety limits of the time-varying fields in MPI will also impact the imaging quality and speed.

Previous studies have shown that magnetostimulation is the main safety concern for drive field frequencies of up to 150 kHz [19, 20, 21]. One important result of these MPI human subject experiments was that the stimulation thresholds decrease with increasing frequency [19], and that the thresholds depend on the direction of the drive field [20, 21, 22]. Another result was that, independent of frequency, the magnetostimulation thresholds decreased with increasing pulse duration, and stabilized for pulse durations longer than approximately 20 ms [23].

In this chapter, we investigate the effects of duty cycle on magnetostimulation thresholds for the drive field in MPI. We perform human subject experiments on six healthy subjects at six different duty cycles, ranging from 5% to 100% duty cycle at 25 kHz. We show that the magnetostimulation thresholds first decrease and then increase with increasing duty cycle, and that the stimulation thresholds at 100% duty cycle are significantly higher than the ones at lower duty cycles. This result has promising implications, as operating at full-duty-cycle drive field would be desirable for rapid imaging purposes.

3.2 Methods

We designed and conducted human subject experiments, approved by Bilkent University Ethics Committee. Our aim was to determine the relationship between duty cycle and magnetostimulation thresholds. All experiments were performed at a single frequency of 25 kHz, to determine the magnetic field amplitudes where the PNS sensations first become discernable. A total of six subjects were tested on the upper arm. The subjects described the magnetostimulation sensation as a twitching or tingling sensation at different intensities and at different locations on their arms. The subjects did not report any pain or discomfort during the study.

3.2.1 Magnetostimulation Setup

Magnetostimulation thresholds were tested with a solenoidal coil on the upper arm of the subjects (see Figure 3.1). This solenoid had a bore size of 11 cm in diameter and 17 cm in length with greater than 95% field homogeneity in a 7 cm-long region, as previously described [19, 23]. The measured magnetic field amplitude was 410 μT/A at the center of the coil.

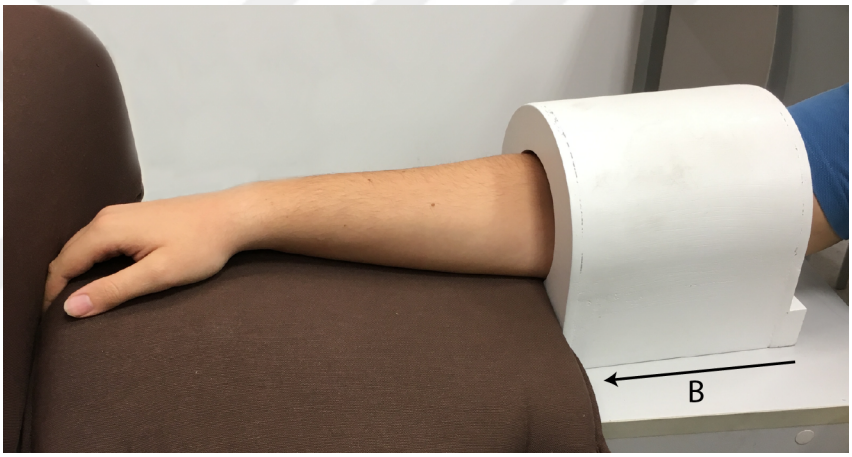

Figure 3.1: A solenodial coil was used to test magnetostimulation limits in the human upper arm with field homogeneity greater than 95% in the axial direction in a 7 cm-long region (magnetic field direction shown with an arrow).

The amplitudes and duty cycles of the magnetic pulses were controlled via MATLAB, using a data acquisition module (NI USB-6363, National Instruments, Austin, TX) that sent the pulse shapes to the power amplifier (AE Techron 7224, AE Techron, Elkhart, IN). At the power limits of the amplifier, the maximum magnetic fields that could be generated varied from 72 mT-pp at 5% duty cycle to 62 mT-pp at 100% duty cycle. A Rogowski AC current probe (PEM, LFR 06/6/300, Nottingham, UK) was used to measure the current on the solenoid during each active interval. These measured current values were multiplied by the 410 μT/A sensitivity of the coil to record the magnetic field amplitudes. This procedure provided a real-time measurement of the magnetic field in the solenoid.

3.2.2 Adjusting Duty Cycle

For testing duty cycle dependence, the experiments required the following conditions: (1) the subject must have enough time to report a magnetostimulation sensation, (2) the sensations must be sufficiently isolated in time to avoid interference between neighboring repetition times, (3) the experiment must allow testing a wide range of duty cycles, and (4) the entire experiment must fit within 20-30 minutes to keep the subject engaged. The first two conditions necessitated the use of an idle period to give the subjects time to report stimulation sensations and to enable them to distinguish each repetition period. The third condition required the active interval for applying magnetic pulses to be as long as possible, while the fourth condition required the overall repetition time to be as short as possible.

An initial test on a single subject was performed to determine the overall repetition time. During this test, we applied 100-ms duration pulses at 2-, 3-, and 4-second repetition times. Subject responses showed less than 1% variation among these three repetition times (results not shown). Hence, considering all four conditions listed above, an overall repetition time of 4 seconds was chosen, where the magnetic pulses were applied during the first 2 seconds (active interval, T_{active}), followed by an idle 2-second resting interval to allow the subject to report stimulation and for the nerves to rest. For determining the duty cycle, we have taken T_{active} as reference. Hence, a continuous magnetic pulse applied throughout T_{active} corresponded to a 100% duty cycle case.

Next, since earlier experiments on the duration dependence of magnetostimulation limits revealed that the thresholds stabilize for pulses longer than 20 ms [23], a pulse duration of $T_{\text{pulse}} = 100$ ms was chosen (see Figure 3.2a). The experiment was designed to include six different duty cycles (5%, 10%, 25%, 50%, 75% and 100%) at 25 kHz. Duty cycle, D, was defined as follows:

$$D = \frac{N_{\text{pulse}} \times T_{\text{pulse}}}{T_{\text{active}}} \times 100 \tag{3.1}$$

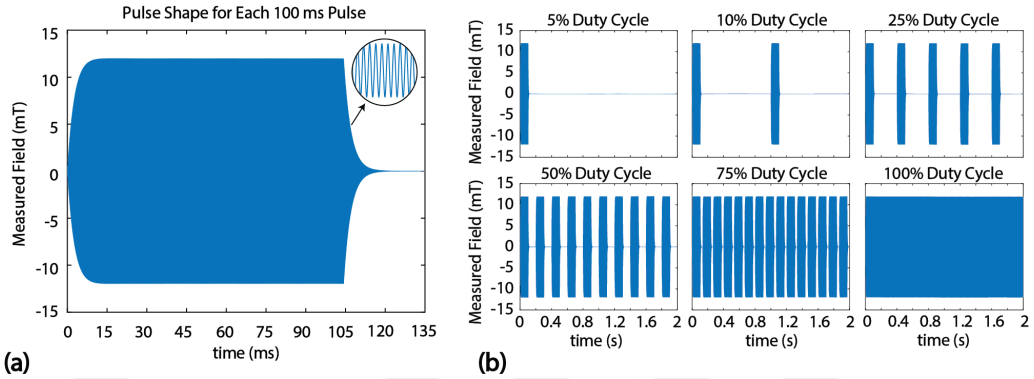

Figure 3.2: Six different duty cycles were tested at 25 kHz. **(a)** Due to inductive/capacitive effects of the experimental setup, each measured pulse of 100-ms duration displayed non-zero ramp up/down times. **(b)** The measured fields for the duty cycles used here: 5%, 10%, 25%, 50%, 75%, and 100% duty cycles. The duration of the active interval was 2 seconds.

where N_{pulse} is the number of equidistant, equal-amplitude 100-ms pulses applied during an active interval (see Figure 3.2.b). In the 100% duty cycle case, a continuous pulse was applied during the entire active interval.

Due to the inductive/capacitive effects in the experimental setup, we observed non-zero ramp up and ramp down times (see Figure 3.2.a).Here, we did not aim to reduce these ramp up/down times, as they were less than 15 ms in duration. The remaining 70 ms of the pulse had a flat envelope, safely overcoming any pulse duration effect that may stem from utilizing short pulses [23]. Here, we calculated the resulting duty cycles directly from the measured magnetic fields [31]:

$$D_{\text{meas}} = \left[\frac{P_{\text{meas}}}{P_{100\%}}\right] \times 100 \tag{3.2}$$

$$= \left[\frac{B_{\text{RMS}}}{B_{\text{peak}}/\sqrt{2}}\right]^2 \times 100 \tag{3.3}$$

$$= \left[\frac{1}{T_{\text{active}}} \int_0^{T_{\text{active}}} B^2_{\text{meas}}(t)dt\right] \frac{2}{\max^2(B_{\text{meas}})} \times 100 \tag{3.4}$$

These calculations are valid for the case of a flat-envelope sinusoidal drive field, as utilized in our experiments. Here, RMS refers to the root-mean-squared value

of the measured magnetic field, calculated via integrating over the entire T_{active} period. Accordingly, we found 5.1%, 10.2%, 25.4%, 50.8%, 76.4%, and 99.8% for the duty cycles, indicating a close match to the targeted values.

3.2.3 Human Subject Experiments

A total of six healthy male subjects were recruited, after screening for safety considerations (i.e., metallic implants, metal objects, pacemakers, etc.). The mean and standard deviations for the age, weight, and height of the subjects were 26±3 years, 86±12 kg and 181±5 cm. Each subject was tested 3 times on different days, with a total of 18 experiments conducted. Each experiment lasted approximately 25-30 minutes. Subjects were in a seating position with their upper arms inside the solenoidal coil, wearing an over-the-head earmuff to help them concentrate on the experiment. They were instructed to click a mouse button whenever they felt a stimulation sensation.

The order in which the duty cycles were tested was randomized at the beginning of each experiment. The first part of the test for each duty cycle started from a low magnetic field amplitude. Then, the field amplitude was slowly increased to determine an approximate threshold level, B_{center}, from the subject's responses. Next, a secondary test was performed to more accurately determine the threshold level. The field amplitudes in this secondary test were chosen in random order to avoid any biasing and hysteresis effect [19]. Here, the field amplitudes were randomized in the ±15% range of B_{center} with a step size of 1% of B_{center}. For each repetition time, the response of the subject was recorded together with the measured field amplitude. A numeric value of "1" was assigned to stimulation response (as reported by the subject via a mouse click), and a numeric value of "0" was assigned if the subject remained unresponsive (see Figure 3.3). This two-step procedure was repeated at each duty cycle. At the end of the experiment, the subject was asked to describe the stimulation sensation and report the approximate stimulation location on their arm.

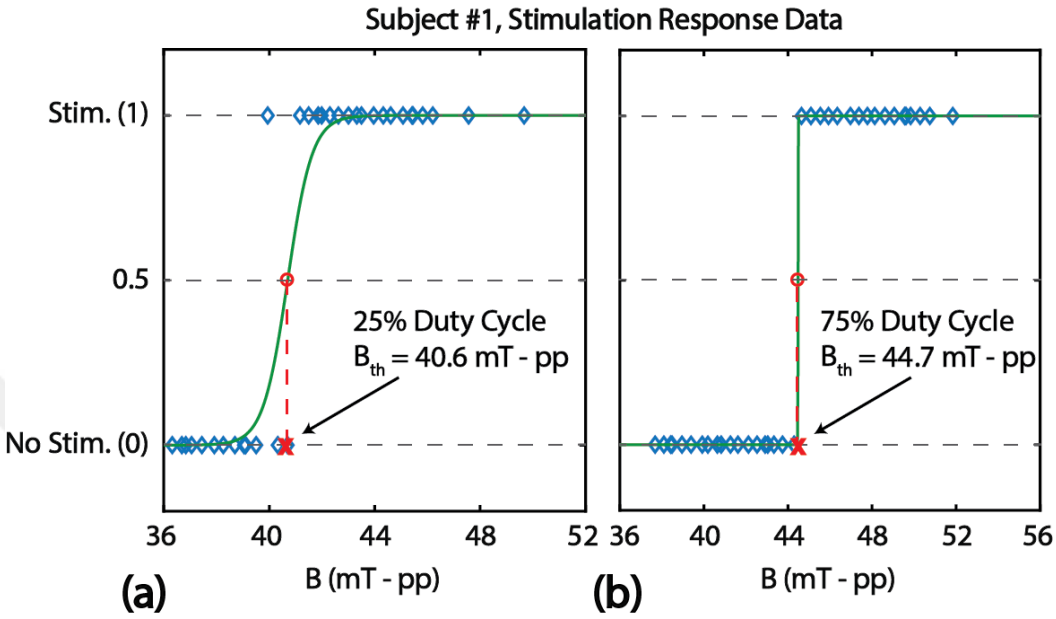

Figure 3.3: Stimulation response data for Subject #1 for 25% and 75% duty cycles at 25 kHz. Blue diamonds represents the subject's responses: "1" denotes that the subject felt a stimulation sensation and "0" denotes that the subject did not experience stimulation. The green curves represent fitted sigmoid functions, and red circles denote the estimated threshold levels. **(a)** Soft transition (W = 0.23 mT-pp) with B_{th} = 40.6 mT-pp at 25% duty cycle. **(b)** Sharp transition (W = 0.0023 mT-pp) with B_{th} = 44.7 mT-pp at 75% duty cycle. In these example data sets, subject's threshold level increased from 40.6 mT-pp at 25% duty cycle to 44.7 mT-pp at 75% duty cycle.

3.2.4 Data Analysis

Similar to our previous studies [19, 23], we modeled the magnetostimulation threshold as a probabilistic parameter to allow for inconsistencies in subject responses. Accordingly, we used a cumulative distribution function (CDF) given by a sigmoid curve

$$F(B) = \left(1 + e^{\frac{-(B-B_{\text{th}})}{W}}\right)^{-1} \tag{3.5}$$

Here, B (mT-pp) is the peak-to-peak magnetic field strength, B_{th} (mT-pp) is the 50% crossing of the sigmoid curve (i.e., the determined stimulation threshold),

and W (mT-pp) is the transition width with smaller W representing sharper transitions. At each duty cycle, the subject's responses were fitted to this sigmoid curve via a Levenberg-Marquardt nonlinear least-squares regression, to yield B_{th} and W. Example stimulation-response data are shown in Figure 3.3 for Subject #1 at two different duty cycles. Figure 3.3a shows a soft transition case at 25% duty cycle with $W = 0.23$ mT-pp due to a few inconsistent responses from the subject. On the other hand, Figure 3.3b shows a sharp transition case at 75% duty cycle with $W = 0.0023$ mT-pp, without any inconsistent responses.

For statistical analysis purposes, the data from each experiment was first normalized by the mean threshold within that experiment. Next, the normalized curves from all 3 experiments for a subject were averaged. This procedure was repeated for all subjects. Finally, a paired Wilcoxon signed rank test was performed to test whether the subjects' responses were significantly different at different duty cycles.

3.3 Results

Figure 3.4a shows the magnestostimulation thresholds as a function of duty cycle for a single subject (Subject #1), for three repetition experiments performed on different days. While the overall trend remains the same, the magnetostimulation thresholds show slight variations among the three repetitions, potentially due to differences in the positioning of the subject's arm within the coil. To better observe the overall trend, we normalized the data from each experiment by the mean magnetostimulation threshold within the corresponding experiment. The normalized curves plotted in Figure 3.4.b show that the magnetostimulation thresholds first decrease and then increase with increasing duty cycle. In all three experiments, the 100% duty-cycle cases display the highest stimulation thresholds.

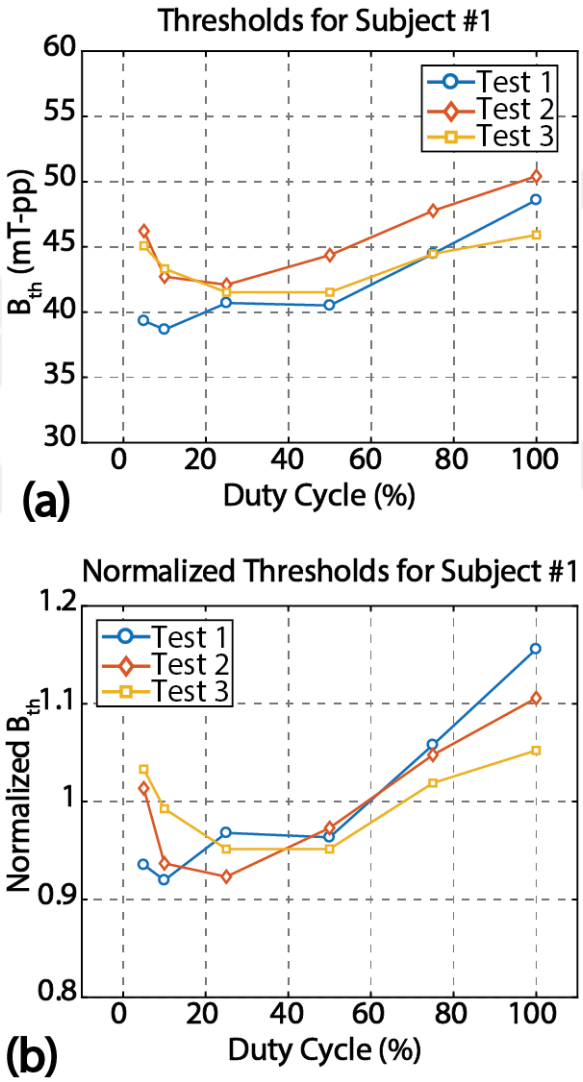

Figure 3.4: **(a)** Magnetostimulation threshold as a function of duty cycle for three different experiments on Subject #1. **(b)** Magnetostimulation thresholds normalized by the mean threshold value for each experiment. In all three experiments, the highest threshold levels were reached at 100% duty cycle.

Figure 3.5 displays the normalized magnetostimulation thresholds for all subjects (N = 6) using all 18 experiments. The plotted curve shows the mean thresholds of all 6 subjects and the error bars denote the standard errors to reflect inter-subject variations. Accordingly, the magnetostimulation thresholds first decrease and then increase with increasing duty cycle, reaching a peak value at 100% duty cycle. The thresholds at 100% duty cycle are approximately 6% higher than those at 5% duty cycle, and approximately 8% higher than those at the 10% to 75% duty cycles. Our statistical analysis also showed that the thresholds at 100% duty cycle were significantly higher than those at lower duty cycles (p¡0.031, paired Wilcoxon signed rank test). In addition, the thresholds at 5% duty cycle were significantly higher than those at 10% duty cycle (p¡0.031, paired Wilcoxon signed rank test). There were no statistically significant differences among other duty cycles.

3.4 Discussion

This chapter investigated the effects of duty cycle on magnetostimulation thresholds for the drive field in MPI at 25 kHz. The human-subject experiments revealed that threshold levels first decrease with increasing duty cycle, then increase again and reach a maximum at 100% duty cycle. Accordingly, this full-duty-cycle case yielded up to 8% higher thresholds than at lower duty cycles. These results suggest that the effect of duty cycle on magnetostimulation thresholds is relatively small when compared to the effects of frequency [19] or pulse duration [23]. Having only a small variation in thresholds at different duty cycles is a promising result in itself, since different imaging applications may require the usage of different duty cycles. Having higher thresholds for the full duty cycle case is a further encouraging result, as it is desirable to operate at 100% duty cycle to minimize the total scan time, e.g., by using a continuous drive field together with a focus field that covers a wide imaging FOV [32].

In the literature, there has been numerous studies on finding the optimum duty cycle for electrical stimulation used for the purposes of muscle rehabilitation and

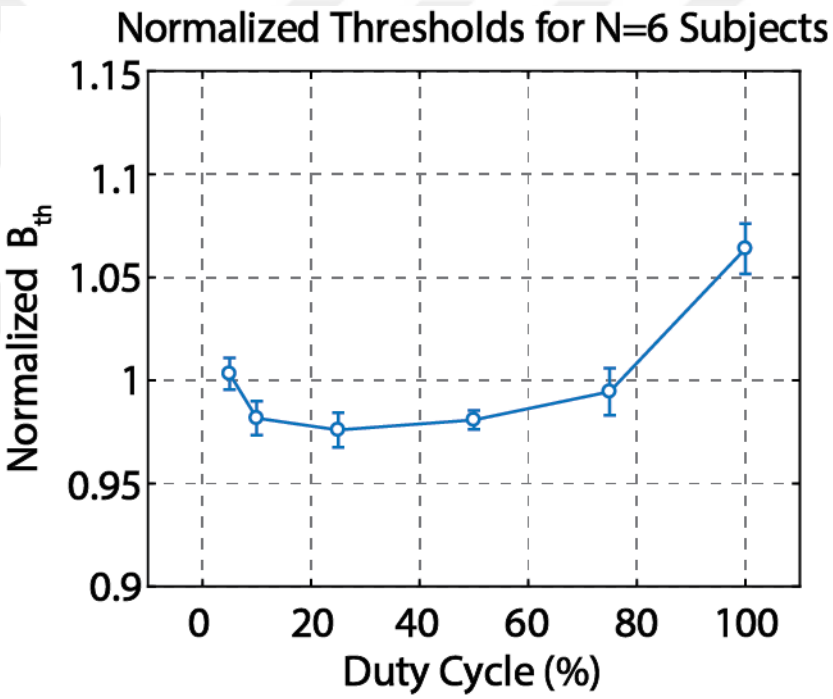

Figure 3.5: Normalized magnetostimulation thresholds as a function of duty cycle for all subjects ($N = 6$), using all 18 experiments. The curve gives the mean thresholds and the error bars denote the standard errors to reflect intersubject variations. Magnetostimulation limits first decrease with increasing duty cycle, and then increase to reach a peak value at 100% duty cycle.

pain control [33, 34, 35]. These studies looked at muscle torque production by using alternating currents from 0.5 kHz to 20 kHz, and unanimously observed that the stimulation efficiency was the highest at approximately 20% duty cycle. Interestingly, these studies were conducted under very different conditions than ours. First, an electrical stimulation was utilized instead of magnetic stimulation. More importantly, the duration between bursts was set to 50 Hz (i.e., 20 ms interval), and the burst duration was varied. Despite these major differences, their findings are consistent with the results of our experiments, as we observed that 25% duty cycle had the lowest magnetostimulation thresholds (the closest to 20% duty cycle among the values that we tested). According to these electrical stimulation studies, the threshold for nerve excitation decreases with multiple bursts of pulses or with prolonged burst durations, which explains the initial decline in the threshold vs. duty cycle curve. However, extended durations or bursts may eventually decrease the response of the nerves due to synaptic fatigue from repetitive action potentials [34]. In fact, during our human-subject experiments, we visually observed that the muscles at the location of magnetostimulation remained contracted throughout the entire 2 s pulse duration for the 100% duty cycle case, which could cause tiredness or numbness in the nerves.

In our experiments, the 5% duty-cycle case corresponded to a single pulse with 100 ms pulse duration, and the 100% duty-cycle case corresponded to a single pulse with 2 s pulse duration (see Figure 3.2.b). A previous work on the relationship between pulse duration and magnetostimulation thresholds showed that, independent of operating frequency, the threshold levels were stabilized for pulses longer than 20 ms [23]. Hence, one would expect the 5% and 100% duty cycle cases to yield the same magnetostimulation threholds. Interestingly, this was not the case in our results, as 100% duty cycle showed approximately 6% higher thresholds. One potential explaination for this discrepancy is that the previous work investigated pulse durations of upto 125 ms and not further.

During our preliminary experiments, we conducted experiments on both the lower arms and upper arms of the subjects. Except for a few subjects, the power amplifier used in this work did not have sufficient power to induce magnetostimulation on the lower arm (results not shown). On the other hand, the same

subjects experienced magnetostimulation at the same magnetic field levels when tested on their upper arms. This result is consistent with the previous work, which showed that magnetostimulation limits decrease with increasing body part size [19]. While the upper arm proved to be an easier location for inducing stimulation, the limits of the power amplifier prohibited us from recruiting female subjects, whose upper arms are relatively smaller in diameter. However, we do not expect there to be any gender differences in the duty-cycle effects described in this chapter, except for the global scaling of the absolute magnetostimulation limits.

Current MPI scanners utilize drive field frequencies in the range of 10 kHz to 150 kHz [36]. Here, we investigated the effects of duty cycle on magnetostimulation thresholds at 25 kHz only. The previous work on pulse-duration-dependence of nerve stimulations showed that the trends remained the same, independent of operating frequency [23]. Accordingly, we expect the trends for duty cycle dependence to also remain the same at different operating frequencies, which remains to be shown experimentally.

Chapter 4

Effects of Fat & Water Ratio on Magnetostimulation Thresholds

4.1 Introduction

The previous chapter showed that the duty cycle of the drive field has a relatively small effect on magnetostimulation thresholds, when compared to frequency and body part size. During the duty cycle experiments presented in this thesis, I observed an interesting phenomenon: subjects with similar arm sizes sometimes had significantly different magnetostimulation thresholds. The main difference between these subjects was observed to be their muscularities. A previous study that investigated the effect of physiological parameters concluded that body fat percentage did not have any significant correlation with the thresholds [24]. That study was performed on the torso and the fat layer thickness was measured using skin-fold measurement with a skin caliper, which may not provide accurate fat percentage values [24]. Therefore, this part of the thesis investigated whether magnetostimulation thresholds depend on the fat percentage of the body part of interest via experiments on the human arm and fat percentage measurements on MRI.

4.2 Methods

We designed and conducted human-subject experiments approved by Bilkent University Ethics Committee. The purpose of the study was demonstrating the effects of fat/muscle ratio on magnetostimulation thresholds. All experiments were conducted at a single frequency of 25 kHz. A total of ten healthy male subjects were recruited, after screening for safety considerations (i.e., metallic implants, metal objects, pacemakers, etc.). The mean and standard deviations for the age, weight, and height of the subjects were 26±2 years, 82±13 kg and 181±5 cm. Each subject was tested 3 times on the same day, with a total of 30 experiments conducted for magnetostimulation experiments. Subjects described the sensations as twitching or tingling on different locations of the upper arm. The subjects did not report any pain or discomfort during the magnetostimulation study. Next, MRI scan of each subject was performed with a 3T Siemens Magnetom Trio MRI scanner to image fat & water tissues separately.

4.2.1 Magnetostimulation Threshold Experiments

To measure the magnetostimulation thresholds, the same setup described in Section 3.2.1 was used. During the experiments, the subjects placed their arms inside the solenoid coil. Since previous work had shown that the duration effects of the applied pulses stabilize beyond 20 ms durations, 100 ms pulses were chosen as shown in Fig. 4.1. The frequency of the applied pulses was 25 kHz. After each pulse, 2 seconds of idle intervals were placed to provide a response time for the subjects. The remaining details of the experiments were kept the same as in Section 3.2.1. After determining the magnetostimulation threshold, the subjects were asked to remove their arms from the solenoid coil and rest for a few minutes. They were then asked to place their arm in approximately the same position, and the procedure was repeated. In total, each subject was tested 3 times to determine intra-subject variations. Each test lasted around 3 minutes.

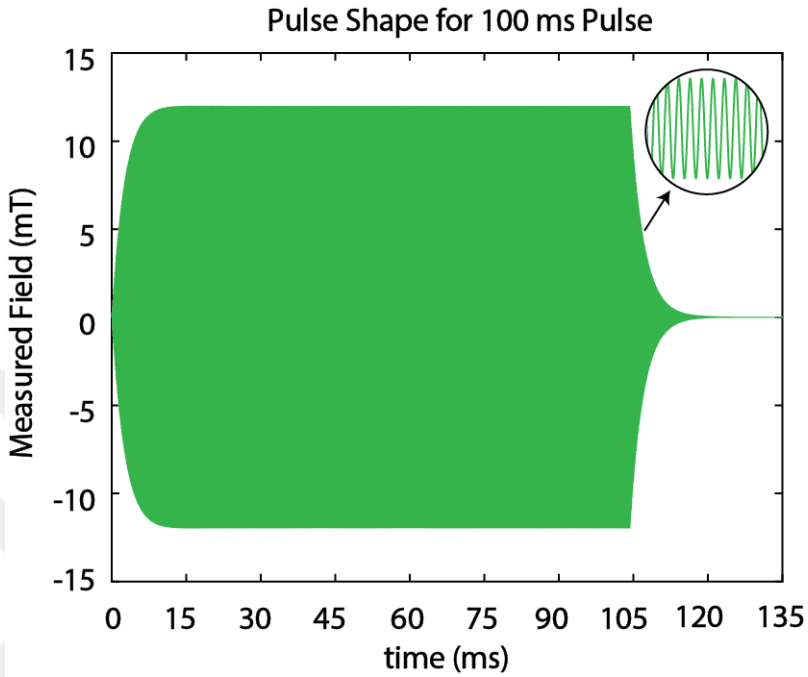

Figure 4.1: A 100 ms pulse was applied at each repetition. Due to inductive/capacitive effects of experimental setup, each measured pulse of 100-ms duration displayed non-zero ramp up/down times. The pulses were repeated at 4-second intervals.

4.2.2 MRI Experiments

MRI experiments were performed using a 3T Siemens Magnetom Trio MRI scanner and a spine matrix receive coil. Subjects were placed in the scanner in head-first prone position, while they extended one arm beyond their heads. The arm that was extended was the one tested during magnetostimulation experiments. To help localize the correct imaging position, a fiducial marker was placed a few cm away from the mid-upper arm area. This location was where most subjects reported feeling the stimulation sensations. A two-point Dixon method [37, 38] was used to acquire fat and water images, separately. The imaging parameters were: TR = 5.27 ms, $TE1$ = 2.45 ms, $TE2$ = 3.675 ms, flip angle = 9^o, $FOV = 380x285mm^2$ and matrix size = $320x240$, 32 s total scan time.

4.3 Data Analysis

The probabilistic model described in Section 3.2.4 was used to determine magnetostimulation thresholds. Example stimulation response data of Subject #1 are shown in Fig. 4.2

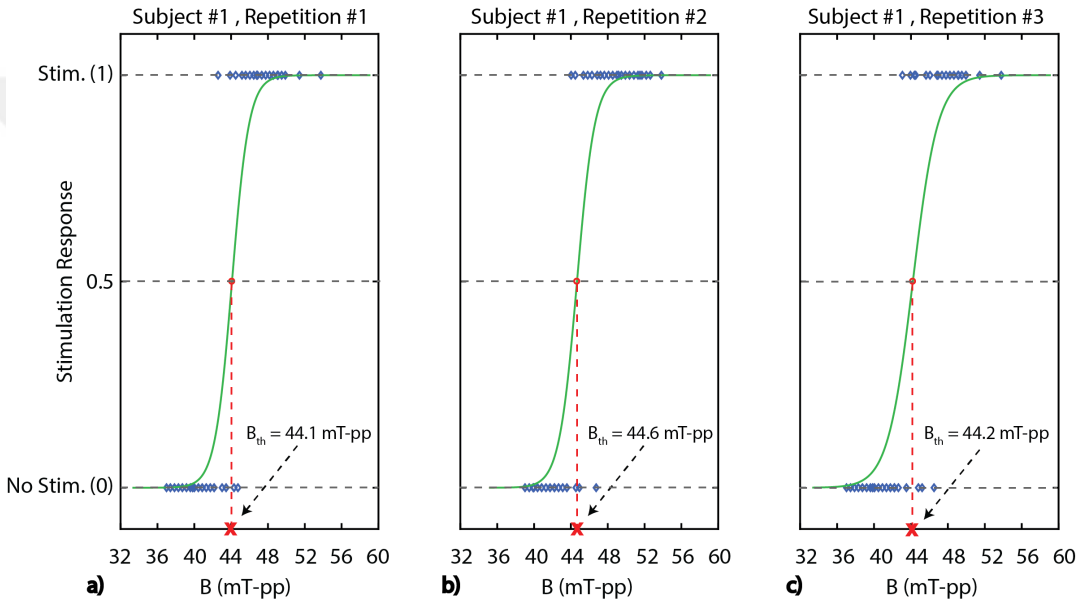

Figure 4.2: Stimulation response data for Subject #1 for 3 repetitions. Blue diamonds represents the subject's responses: "1" denotes that the subject felt a stimulation sensation and "0" denotes that the subject did not experience stimulation. The green curves represent fitted sigmoid functions, and red circles denote the estimated threshold levels. (a) Repetition #1, soft transition (W = 0.46 mT-pp) with B_{th} = 44.1 mT-pp (b) Repetition #2, soft transition (W = 0.48 mT-pp) with B_{th} = 44.6 mT-pp (c) Repetition #3, soft transition (W = 0.67 mT-pp) with B_{th} = 44.2 mT-pp.

During the MRI scans, a two-point Dixon method was used to obtain water and fat images separately [37, 38]. This sequence provides two images. One demonstrates water tissue only, while the other shows fat tissue only. First, a region of interest (ROI) of same pixel sizes was selected on each image for each subject. This ROI selection served two purposes: to remove the fiducial marker and any other anatomical parts from consideration, and to centralize the arm region in the image. Next, the water image and fat image were individually normalized by their respective maximum pixel intensities. From these two images,

Canny edge detection algorithm was used via MATLAB [39] to determine the inner and outer rings of the fat image, as shown in Fig. 4.3. To calculate the center of mass for fat and water, the interior regions of the rings were filled as a binary image, as shown in Fig. 4.3. For each filled image, the effective radius was calculated as the mean distance between each point on the ring and the center of mass. This procedure was performed for the inner ring and the outer ring separately, to yield two effective radii per subject. Note that the radius of the inner ring can be considered as the effective radius for muscle tissue.

The ratio of fat and water tissues was calculated via two different methods. In the first method, the sum of the normalized pixel intensities of the fat image was calculated, and divided by that of the water image. In the rest of this chapter, this ratio is labeled as $Fat/Water_{direct}$. Here, the initial individual normalization of fat and water images ensures that the pixel intensities are not biased by T_1/T_2 contrast differences between these two tissue types. However, each image still experiences a shading effect due to spatial variations in coil sensitivities. Hence, a direct summation of the fat image may not correctly estimate the total fat content (same for the water image). Therefore, a second technique was used: the filled inner ring (shown in Fig. 4.3) was taken as a binary representation of the muscle tissue. A binary representation of the fat tissue was then calculated by taking the difference of the filled outer ring and the filled inner ring images (see Fig. 4.3). The ratio of the fat and water tissues, $Fat/Water_{binary}$, was then calculated by summing each binary image and taking their ratio.

In Fig 4.4, upper arm MRI images of all ten subjects are shown with corresponding fat and water images, extracted inner and outer rings, and the filled versions of the inner and outer rings where the red dots represent the center of masses.

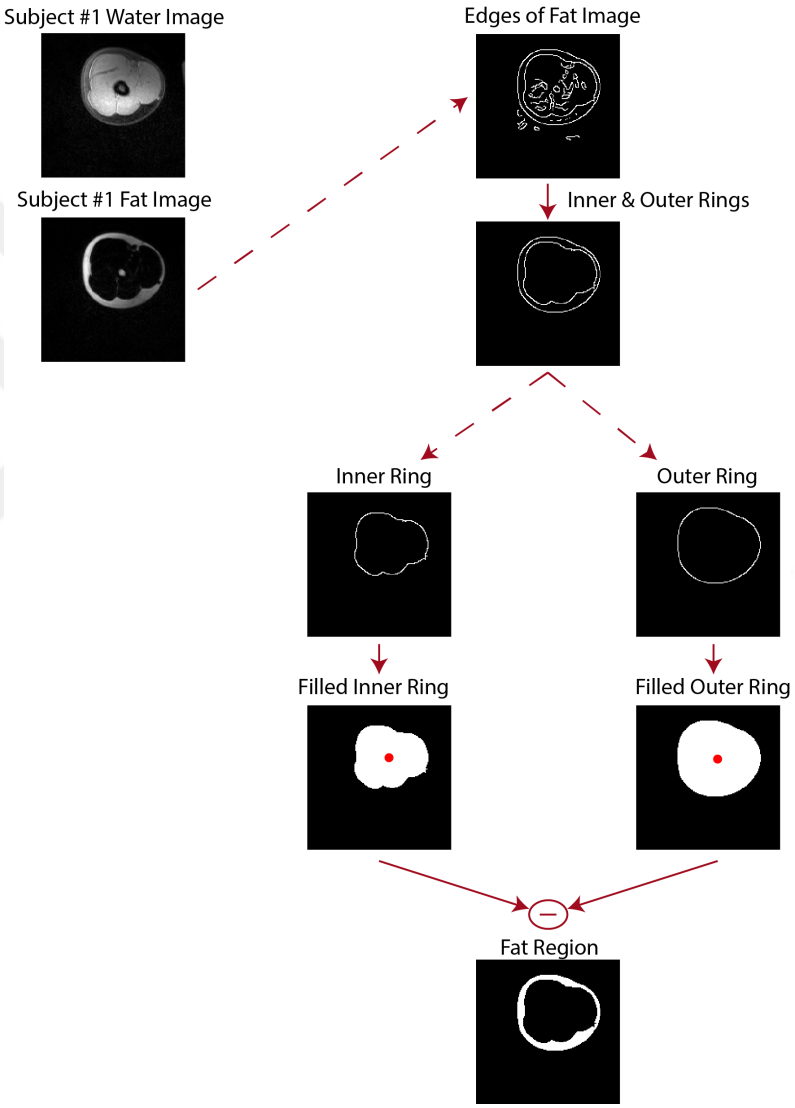

Figure 4.3: Subject #1's Fat and Water Images, corresponding edge of fat image, inner and outer rings from the edge detection, inner ring and filled inner ring representing muscle tissue, outer ring and filled outer ring, calculated fat region from the difference of filled rings are shown. The red dots represent the center of mass points.

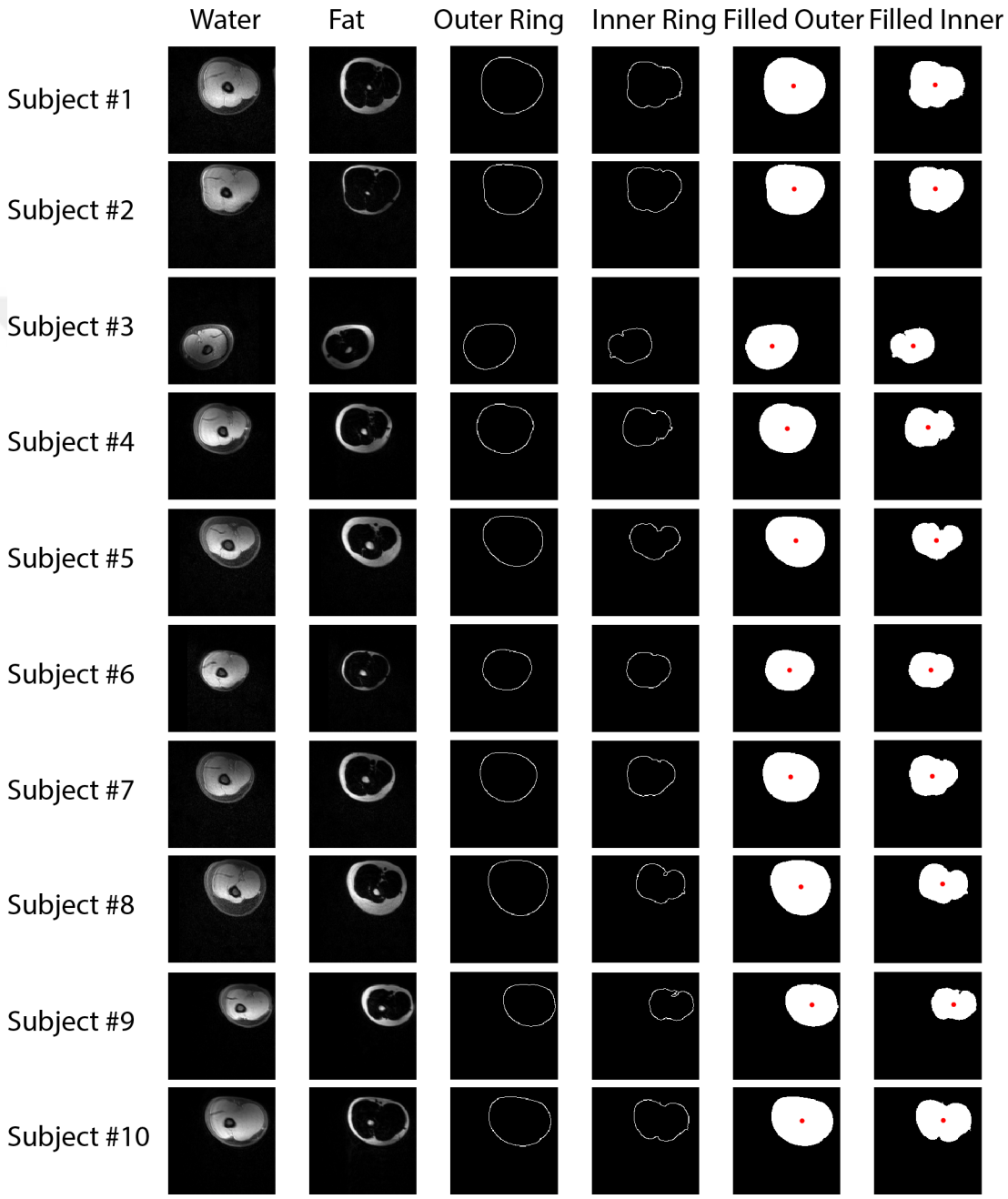

Figure 4.4: Upper arms of all ten subjects. The 1st column represents water images from Dixon method. The 2nd column represents fat images from Dixon method. The 3rd and 4th columns represent outer and inner rings from the edge detection algorithm, respectively. The 5th and 6th columns represent the filled versions of outer and inner rings. The red dots represent the center of mass points.

4.4 Results

Figure 4.5.a shows the magnetostimulation thresholds as a function of repetition for Subject #1, and Fig. 4.5.b shows their normalized versions. This figure shows that, there is a minor 1.3% intra-subject variation for Subject #1, despite the fact that the subject's upper arm was not in exactly the same position. Other subjects had similar results, where the intra-subject variation ranged between 1.3% and 8.6%. For the remainder of the analysis, the mean value of the three repetitions was taken as the magnetostimulation threshold of that subject.

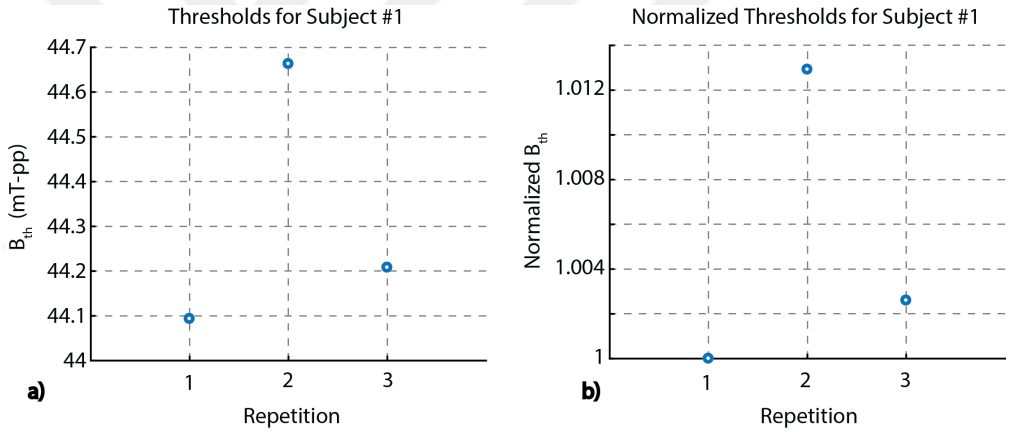

Figure 4.5: (a) Magnetostimulation threshold as a function of repetition for Subject #1. (b) Magnetostimulation thresholds normalized by the minimum threshold value from 3 repetitions.

Figure 4.6 shows the scatter plots of the magnetostimulation thresholds for all 10 subjects, versus various anatomical measures extracted from the MRI images. A linear fit was performed on each scatter plot, shown with orange dashed lines. To measure the linear correlation between each anatomical measure and the magnetostimulation thresholds, Pearson correlation coefficients were computed. Figure 4.6.a shows the linear relationship between the inverse of inner radii and magnetostimulation thresholds, B_{th}. The dashed orange curve represents the fitted relationship between the inverse of inner radius and B_{th}, where a strong correlation can be seen (r=0.774, p=0.009). Furthermore, Fig. 4.6.b shows the linear relationship between the inverse of outer radius and B_{th}, where no significant correlation was observed (r=0.055, p=0.890).

Figure 4.6.c shows the linear relationship between the $Fat/Water_{direct}$ ratio and magnetostimulation thresholds. The dashed orange curve represents the fitted relationship between the $Fat/Water_{direct}$ and B_{th}, where a strong correlation can be seen (r=0.799, p=0.006). Likewise, Fig. 4.6.d shows that there is a strong correlation between $Fat/Water_{binary}$ and B_{th} (r=0.743, p=0.013).

The Pearson correlation coefficients and the corresponding p-values are given in Table 4.1. Note that the Pearson correlation coefficients for the inner and outer radii were calculated between the inverse of the radii and B_{th}.

Metric	Pearson Correlation Coefficient (r)	p-values (p)
$InnerRadius^{-1}$	0.774	0.009
$OuterRadius^{-1}$	0.055	0.890
$Fat/Water_{direct}$	0.799	0.006
$Fat/Water_{binary}$	0.743	0.013

Table 4.1: The linear relationship between the inverse of inner radius and inverse of outer radius and magnetostimulation thresholds, the linear relationship between fat/water and magnetostimulation thresholds are presented. The inverse of the inner radius, $Fat/Water_{direct}$ and $Fat/Water_{binary}$ have strong correlation with magnetostimulation thresholds while the inverse of outer radius shows no significant correlation with the magnetostimulation thresholds.

Figure 4.7.b shows that the linear relationship between $Fat/Water_{direct}$ ratio and magnetostimulation thresholds increases when a subset of subjects for chosen to limit the arm size variation to a maximum of $\pm 10\%$. The minimum selected outer arm radius was 4.62 cm and the maximum selected outer arm radius was 5.2 cm for the 6 selected subjects. The dashed orange curve represents the fitted relationship between $Fat/Water_{direct}$ and B_{th}, where much stronger correlation can be seen (r=0.912, p=0.012) in the case of size selection. The Pearson correlation coefficient was increased from 0.799 to 0.912 in the size selective case.

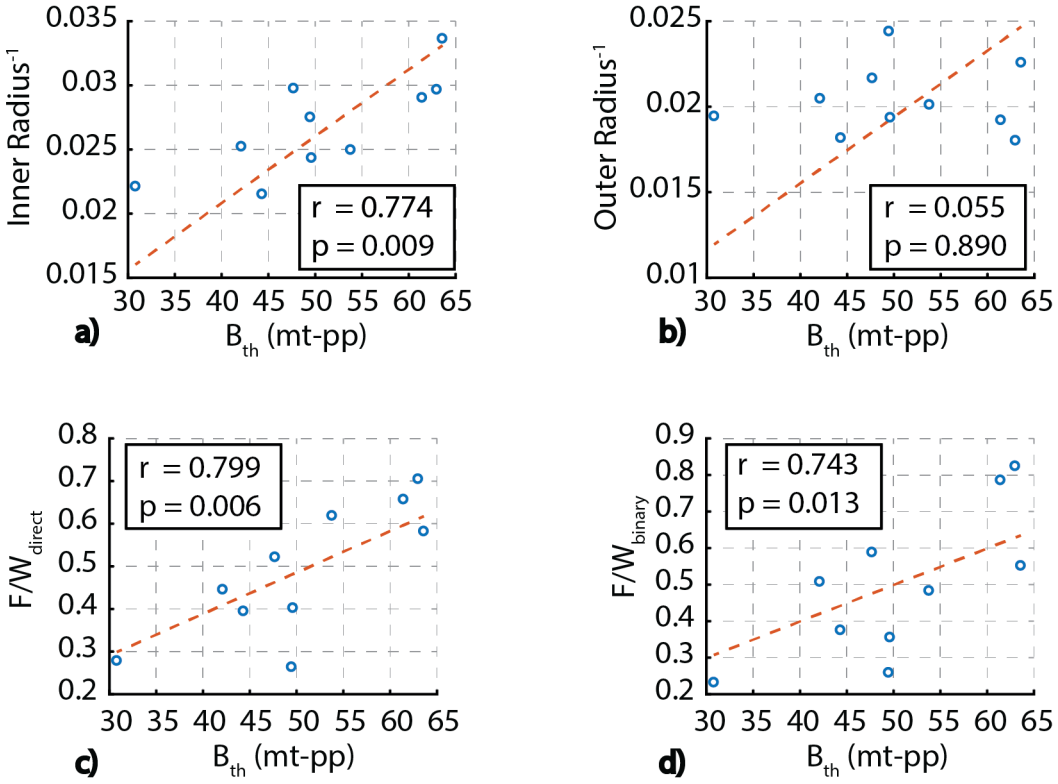

Figure 4.6: a) A strong correlation was found between the inverse of inner radius and magnetostimulation thresholds (r=0.774, p=0.009) b) No significant correlation was found between inverse of outer radius and the thresholds (r=0.055, p=0.890). c) A strong correlation was found between $Fat/Water_{direct}$ and thresholds (r=0.799, p=0.006), where $Fat/Water_{direct}$ represents ratio between the unprocessed fat and water images. d) A strong correlation was found between $Fat/Water_{binary}$ and thresholds (r=0.743, p=0.013), where $Fat/Water_{binary}$ represents ratio between the fat and muscle regions using the filled binary images.

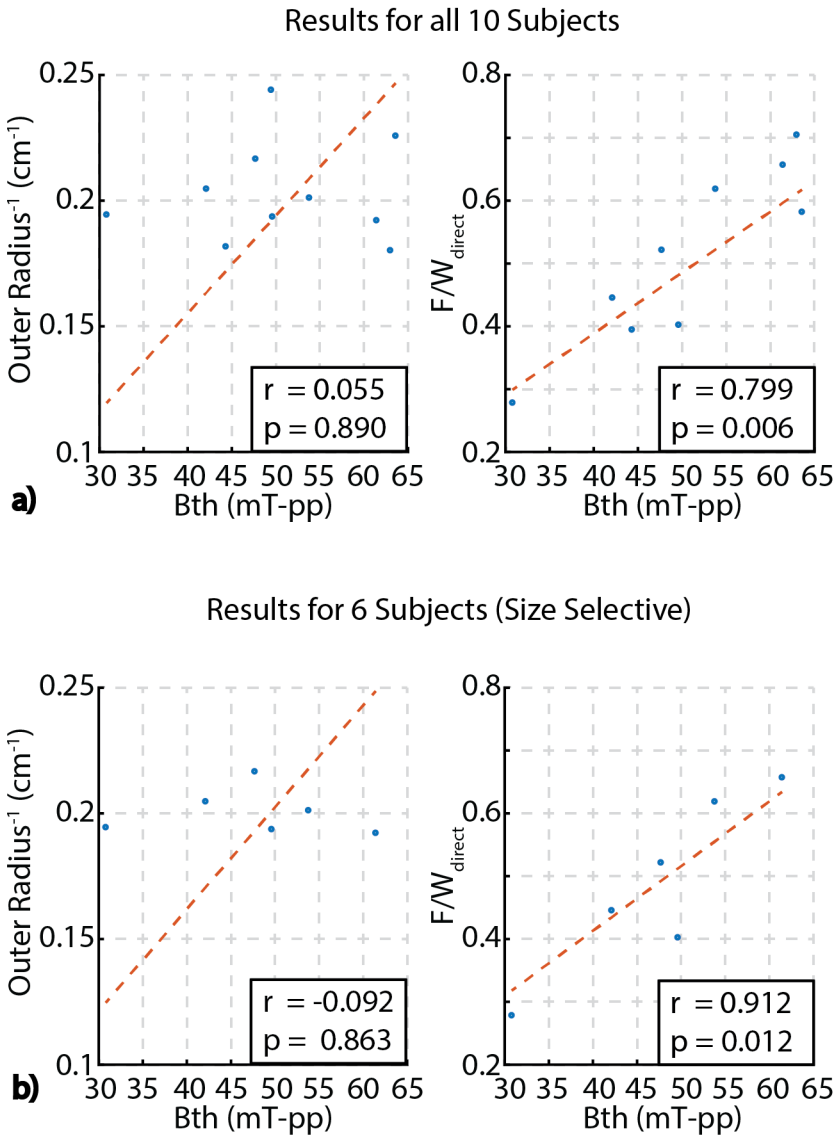

Figure 4.7: a) When results of all 10 subjects were investigated, a strong correlation was found between the $Fat/Water_{direct}$ ratio and magnetostimulation thresholds (r=0.799, p=0.006). b) In the case of selective arm sizes ($\pm$10% variation only within the selected 6 subjects), a stronger correlation (r=0.912, p=0.012) can be seen between the $Fat/Water_{direct}$ ratio to magnetostimulation thresholds.

4.5 Discussion

Strong correlation between the fat/water tissue ratio and magnetostimulation thresholds validated the observations we have made at the beginning. The reasons behind the different magnetostimulation thresholds with similar arm sizes appeared as variations of fat/water tissue ratio and variations of muscularity (inner radius of the arms). To calculate fat/water tissue ratio, two different methods (direct and binary methods) were used, which both yielded a strong correlation between the fat/water ratio and thresholds. In addition, it has been shown for the first time that the fat/water ratio is an important factor for magnetostimulation thresholds. Furthermore, outer radii of the subjects did not reveal a correlation with magnetostimulation thresholds ($r = 0.055$, $p=0.890$), while inner radii showed a significant correlation ($r=0.774$, $p=0.009$). This result implies that the outer fat layer does not have any effect in determining magnetostimulation thresholds, as the PNS sensation is induced on either the nerves or muscles. Furthermore, it was shown that the correlation between the ratio of fat/water and magnetostimulation thresholds increased from $r = 0.799$ to $r = 0.912$ when a subset of subjects with a restriction on arm size were selected.

Interestingly, these results were not the case in a previous work based on correlations of anatomical thresholds to PNS thresholds in MRI [24]. However, their experiments were conducted on human torso where there are much more anatomical variations [24]. Besides, they concluded that there was no significant correlation between PNS thresholds and body size. However, a previous study on both arms and legs of human subjects has shown that there is a strong correlation with the inverse of body part size and magnetostimulation thresholds [19]. For that study, performing the experiments on both the arms and legs provided a bigger variation in radius, which enabled the demonstration of such a strong correlation. That study only considered the outer radius and not the inner radius. In this chapter, we did not see a correlation with the outer radius, as the recruited subjects did not have sufficient variation in the outer radii of their upper arms. Despite this restriction, we observed a strong correlation between the inverse of the inner radius and the thresholds. This result implies that the correlation

between body part size and thresholds is much stronger when the inner radius is considered (i.e., excluding the outer fat region).

For the previous work on the torso, statistical summary of measured data from 17 subjects demonstrated a mean radius of 14.1 cm and a standard deviation of 1.7 cm for the axial area of the torsos [24]. Our measured data from 10 subjects showed a mean radius of 4.9 cm and a standard deviation of 0.46 cm for the axial area of the upper arms. The size selective case in Fig. 4.7 had a mean radius of 4.9 cm but a much lower standard deviation of 0.22 cm for the axial area of the upper arms. Therefore, a restriction on outer radius of the subjects made it easier to observe the correlation between the fat/water ratio to magnetostimulation thresholds. These results imply that the fat/water ratio has a secondary effect on the magnetostimulation thresholds: when subjects with similar apparent sizes are considered, the subjects with higher fat/water ratio will have higher magnetostimulation thresholds. In contrast, one cannot make any predictions on the thresholds based only on the fat/water ratio, as the dominant effect in determining the thresholds is the radius of the body part size.

The results of this chapter can be useful for selecting subject-dependent scanning parameters. By using subject-dependent scanning parameters, MPI can be utilized with higher drive field performance while avoiding magnetostimulation.

Chapter 5

Fast Scanning in MPI

This chapter is based on the publication titled "Rapid Scanning in X-Space MPI: Impacts on Image Quality" O.B. Demirel, D. Sarica, E.U. Saritas, International Workshop on Magnetic Particle Imaging (2016).

5.1 Introduction

Initially, piecewise constant focus fields were used in x-space MPI to cover the field-of-view (FOV) by dividing it into overlapping partial FOVs (pFOV) [3, 8]. Since this step-by-step coverage proved to be time consuming, a linear focus field was utilized in more recent works [25, 26]. Previously, effects of rapid scanning were analyzed for system matrix reconstruction [27], but have not been researched in x-space MPI. Here, we investigate the effects of rapid scanning on image quality for x-space MPI images.

5.2 Materials and Methods

In case of piecewise constant focus field, filtering the fundamental frequency results in a DC loss term (Fig. 5.1.a) [25]. Here, we utilize a linear focus field:

$$H_{focus}(t) = \frac{2B_f}{\mu_0 T_{ramp}} t - \frac{B_f}{\mu_0} \tag{5.1}$$

Here, $B_f \triangleq \mu_0 G.FOV/2$ [T] is the maximum focus field, G [T/m/μ_0] is the selection field, FOV [m] is the total coverage, and T_{Ramp} [s] is the ramp time of the focus field. We also define $S_r \triangleq (2B_f)T_{Ramp}$ [T/s] as the slew rate of the focus field. When S_r is relatively high, fundamental filtering not only causes a DC loss, but also distorts the edges of the reconstructed pFOVs (Fig. 5.1.b). This complicates x-space image reconstruction.

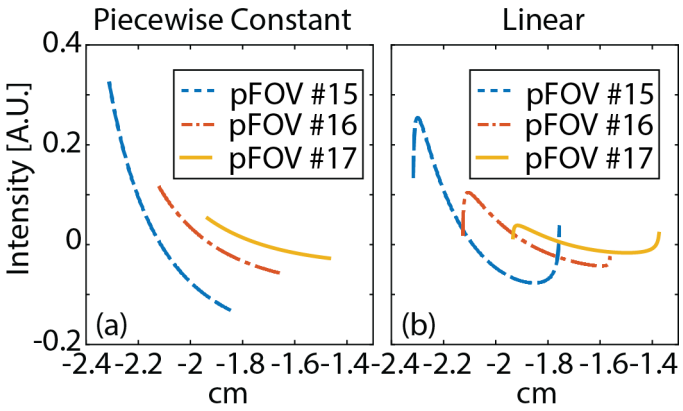

Figure 5.1: Reconstructed images for (a) piecewise constant focus field, and (b) linear focus field (shown for $S_r = 150$ T/s).

Here, we implemented an SNR-optimized reconstruction algorithm that robustly calculates the effective DC loss and stitches images from all pFOVs, even for high S_r values. In this algorithm, each point in a pFOV is weighted by the corresponding squared-velocity of the field-free point (FFP). We developed a custom MPI simulation toolbox in MATLAB to test the effect of S_r on image quality. 7mT-peak drive field at 25 kHz was utilized in accordance with magnetostimulation limits [40]. Gxx=Gzz=3T/m selection field, 10x4cm2 FOV, 25nm

nanoparticle diameter was used, ignoring relaxation effects.

5.3 Results and Discussion

According to our simulations, there are two effects of fast scanning on image quality: overall signal loss and slight resolution enhancement. Fig. 5.2 shows example images from 20 T/s (the safety limit for focus field, adopted from MRI [40]) and 150 T/s. As shown in Fig. 5.2.d, the signal losses at 20 T/s and 150 T/s were 3.5% and 19%, respectively. Interestingly, higher slew rates resulted in slightly better resolution (see Fig. 5.3.b): approximately 1% improvement at 20 T/s and 10% at 150 T/s. It should be noted that this secondary effect may not be valid if relaxation effects are taken into account. Additionally, we observed that linearity and shift invariance holds for slew rates up to 180 T/s. At higher slew rates the image quality suffered considerably (see Fig. 5.4).

Figure 5.5 shows the scanning times with respect to nine different slew rates for a 5cm x 5cm phantom with following scanning parameters: Frequency = 25 kHz, Drive Field Amplitude = 14 mT-pp, Number of line scanned along x-axis = 101. This figure shows that scanning times can go below 100 ms for higher slew rates greater than 75 T/s.

To reduce the scanning times, different scanning trajectories were utilized in MPI systems [41, 26]. However, conventional methods (piecewise constant focus field) to cover the FOV are time consuming. This chapter demonstrated that the scanning times can be reduced by using linear focus fields while human safety limits are not exceeded. Furthermore, this chapter showed that image quality was preserved even though human safety limits are exceeded (slew rates greater than 20 T/s). Despite the distorted edges of pFOVs due to linearly increasing focus fields, x-space image reconstruction with DC recovery is capable enough to preserve image quality [8]. Besides, linear focus fields revealed signal loss and slight resolution improvement which is an promising effect for imaging applications.

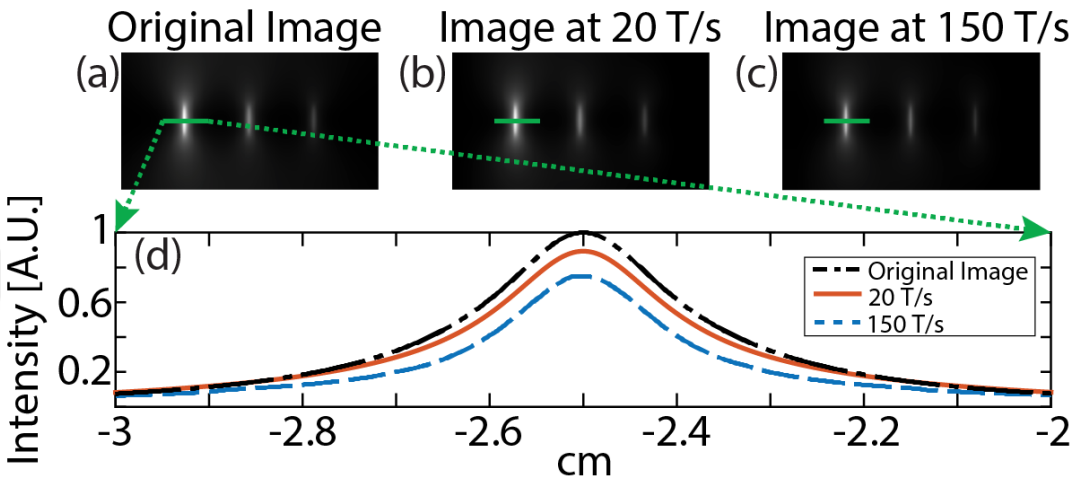

Figure 5.2: Images at various scanning speeds. (a) Original image for piecewise constant focus field. (b) Image for $S_r = 20$ T/s. (c) Image for $S_r = 150$ T/s. (d) Zoomed in 1D cross-section.

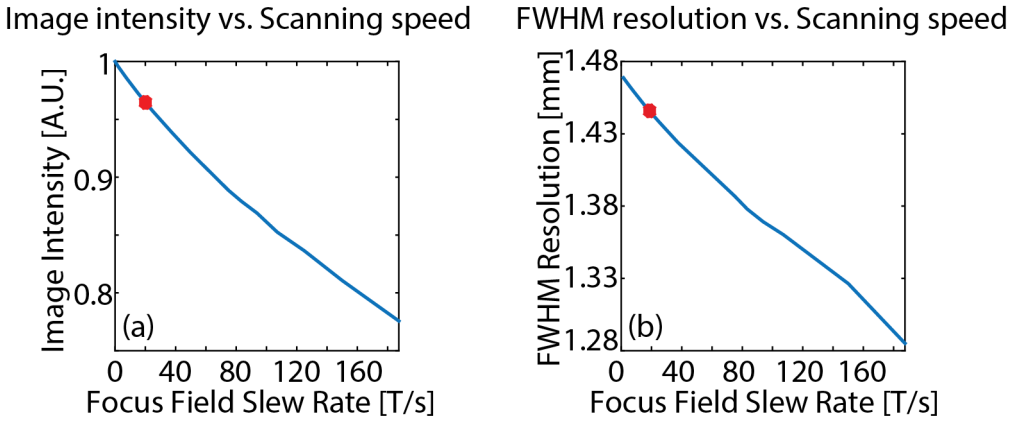

Figure 5.3: Impact of fast scanning on (a) image intensity and (b) FWHM resolution, given as a function of focus field slew rate.

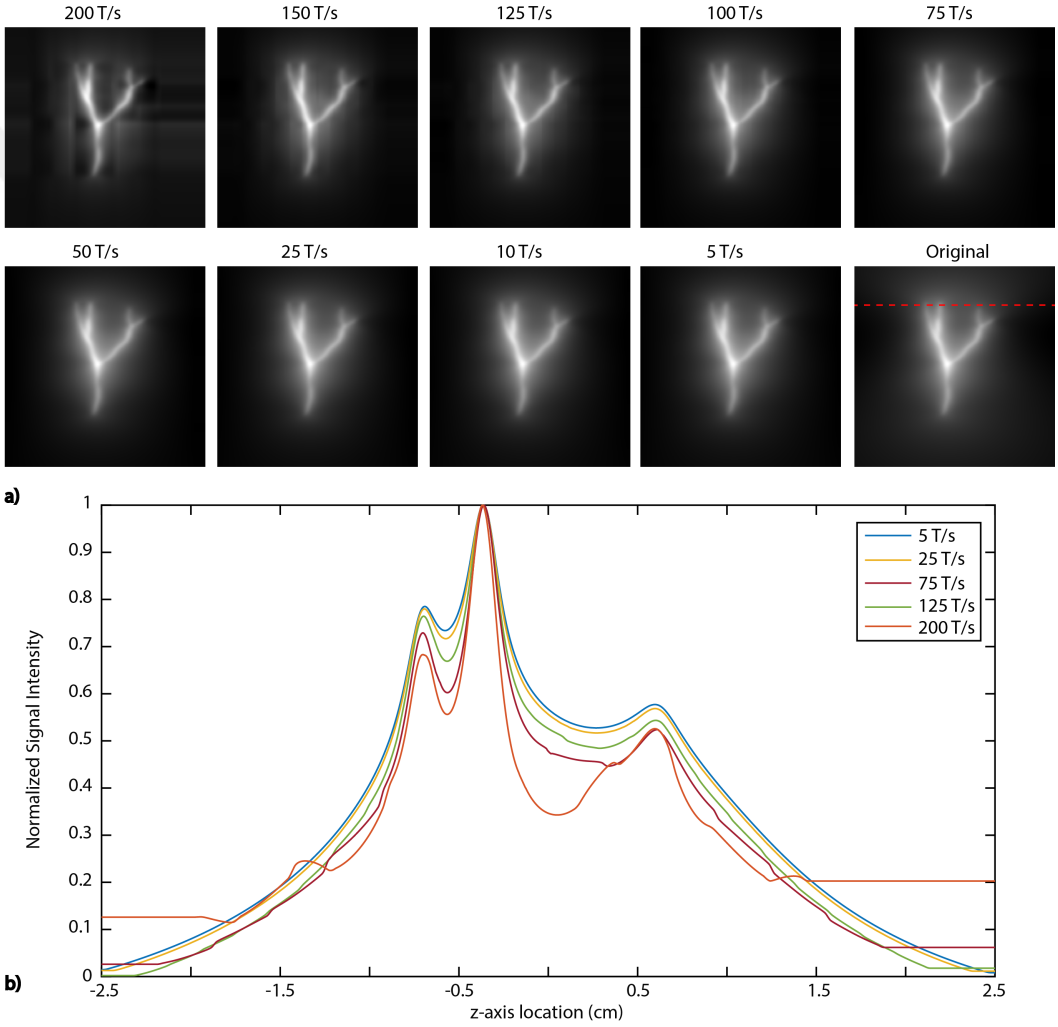

Figure 5.4: a) Images with respect to different slew rates. All scanning parameters are same for all nine images. b) A line shown with a dashed red line on original image was plotted for some slew rates to show image qualities.

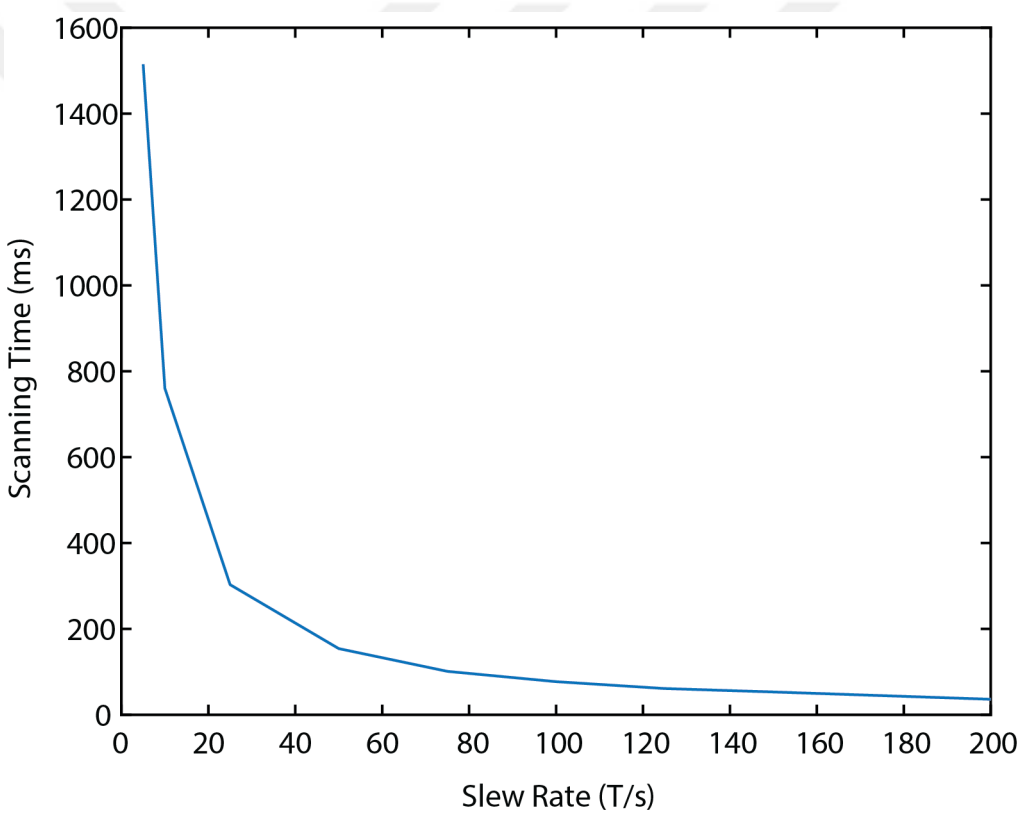

Figure 5.5: Scanning time with respect to the different slew rates for the image presented in Fig. 5.4.

Chapter 6

Conclusion

In this thesis, it was shown with human-subject experiments that the magnetostimulation thresholds first decrease and then increase with increasing duty cycle, reaching a peak value at 100% duty cycle. These results have promising consequences for rapid imaging in MPI, since operating at full duty cycle would be the preferred mode for most imaging applications.

Furthermore, it was demonstrated that fat/water tissue ratio has a significant correlation with magnetostimulation thresholds. In addition, the inner radius of the arm (i.e., the effective radius for the muscle tissue) has a strong correlation with magnetostimulation thresholds. These results suggest that the subject dependent scanning parameters can be utilized to increase the performance of drive fields in MPI while avoiding magnetostimulation.

Finally, it was demonstrated that image quality is preserved when slew rates are within the human-subject safety limits of MPI. When slew rate is further increased, the dominant effect is an overall signal loss. Investigating the effects of nanoparticle relaxation and SNR remains as future work.

Bibliography

[1] B. Gleich and J. Weizenecker, "Tomographic imaging using the nonlinear response of magnetic particles," *Nature*, vol. 435, no. 7046, pp. 1214–1217, 2005.

[2] E. U. Saritas, P. W. Goodwill, L. R. Croft, J. J. Konkle, K. Lu, B. Zheng, and S. M. Conolly, "Magnetic particle imaging MPI for NMR and MRI researchers," *Journal of Magnetic Resonance*, vol. 229, pp. 116 – 126, 2013.

[3] P. W. Goodwill and S. M. Conolly, "The x-space formulation of the magnetic particle imaging process: 1-d signal, resolution, bandwidth, snr, sar, and magnetostimulation," *IEEE transactions on medical imaging*, vol. 29, no. 11, pp. 1851–1859, 2010.

[4] E. Yu, M. Bishop, P. W. Goodwill, B. Zheng, M. Ferguson, K. M. Krishnan, and S. M. Conolly, "First murine in vivo cancer imaging with mpi," in *6th International Workshop on Magnetic Particle Imaging (IWMPI 2016): Book of Abstracts*, Infinite Science Publishing, 2016.

[5] B. Zheng, T. Vazin, P. W. Goodwill, A. Conway, A. Verma, E. U. Saritas, D. Schaffer, and S. M. Conolly, "Magnetic particle imaging tracks the long-term fate of in vivo neural cell implants with high image contrast," *Scientific Reports*, vol. 5, no. 14055, 2015.

[6] K. Them, J. Salamon, P. Szwargulski, S. Sequeira, M. G. Kaul, C. Lange, H. Ittrich, and T. Knopp, "Increasing the sensitivity for stem cell monitoring in system-function based magnetic particle imaging," *Physics in Medicine and Biology*, vol. 61, no. 9, p. 3279, 2016.

[7] J. Weizenecker, B. Gleich, J. Rahmer, H. Dahnke, and J. Borgert, "Three-dimensional real-time in vivo magnetic particle imaging," *Physics in Medicine and Biology*, vol. 54, no. 5, p. L1, 2009.

[8] K. Lu, P. W. Goodwill, E. U. Saritas, B. Zheng, and S. M. Conolly, "Linearity and shift invariance for quantitative magnetic particle imaging," *IEEE transactions on medical imaging*, vol. 32, no. 9, pp. 1565–1575, 2013.

[9] C. Stehning, B. Gleich, and J. Rahmer, "Simultaneous magnetic particle imaging (mpi) and temperature mapping using multi-color mpi," *International Journal on Magnetic Particle Imaging*, vol. 2, no. 2, 2016.

[10] K. Murase, M. Aoki, N. Banura, K. Nishimoto, A. Mimura, T. Kuboyabu, and I. Yabata, "Usefulness of magnetic particle imaging for predicting the therapeutic effect of magnetic hyperthermia," *Open Journal of Medical Imaging*, vol. 5, no. 2, p. 85, 2015.

[11] D. Hensley, P. W. Goodwill, R. Dhavalikar, Z. W. Tay, B. Zheng, C. Rinaldi, and S. M. Conolly, "Imaging and localized nanoparticle heating with mpi," in *6th International Workshop on Magnetic Particle Imaging (IWMPI 2016): Book of Abstracts*, Infinite Science Publishing, 2016.

[12] Y. Muslu, M. Utkur, O. B. Demirel, and E. U. Saritas, "Calibration-free relaxation-based multi-color magnetic particle imaging," *arXiv preprint arXiv:1705.07624*, 2017.

[13] E. E. Mason, C. Z. Cooley, S. F. Cauley, M. A. Griswold, S. M. Conolly, and L. L. Wald, "Design analysis of an mpi human functional brain scanner," *International Journal on Magnetic Particle Imaging*, vol. 3, no. 1, 2017.

[14] J. Reilly, "Peripheral nerve stimulation by induced electric currents: Exposure to time-varying magnetic fields," *Medical and Biological Engineering and Computing*, vol. 27, no. 2, p. 101, 1989.

[15] J. P. Reilly, "Maximum pulsed electromagnetic field limits based on peripheral nerve stimulation: application to IEEE/ANSI C95.1 electromagnetic field standards," *IEEE Transactions on Biomedical Engineering*, vol. 45, pp. 137–141, Jan 1998.

[16] P. A. Bottomley and W. A. Edelstein, "Power deposition in whole–body NMR imaging," *Medical Physics*, vol. 8, no. 4, pp. 510–512, 1981.

[17] F. Schmitt, W. Irnich, and H. Fischer, *Physiological Side Effects of Fast Gradient Switching*, pp. 201–252. Berlin, Heidelberg: Springer Berlin Heidelberg, 1998.

[18] W. Irnich and F. Schmitt, "Magnetostimulation in MRI," *Magnetic Resonance in Medicine*, vol. 33, no. 5, pp. 619–623, 1995.

[19] E. U. Saritas, P. W. Goodwill, G. Z. Zhang, and S. M. Conolly, "Magnetostimulation limits in magnetic particle imaging," *IEEE Transactions on Medical Imaging*, vol. 32, pp. 1600–1610, Sept 2013.

[20] I. Schmale, B. Gleich, J. Schmidt, J. Rahmer, C. Bontus, R. Eckart, B. David, M. Heinrich, O. Mende, O. Woywode, J. Jokram, and J. Borgert, "Human PNS and SAR study in the frequency range from 24 to 162 kHz," in *Magnetic Particle Imaging (IWMPI), 2013 International Workshop on*, pp. 1–1, March 2013.

[21] I. Schmale, B. Gleich, J. Rahmer, C. Bontus, J. Schmidt, and J. Borgert, "MPI safety in the view of MRI safety standards," *IEEE Transactions on Magnetics*, vol. 51, pp. 1–4, Feb 2015.

[22] E. Yu, E. U. Saritas, and S. M. Conolly, "Comparison of magnetostimulation limits for axial and transverse drive fields in MPI," in *Magnetic Particle Imaging (IWMPI), 2013 International Workshop on*, pp. 1–1, March 2013.

[23] E. U. Saritas, P. W. Goodwill, and S. M. Conolly, "Effects of pulse duration on magnetostimulation thresholds," *Medical Physics*, vol. 42, no. 6, pp. 3005–3012, 2015.

[24] B. A. Chronik and M. Ramachandran, "Simple anatomical measurements do not correlate significantly to individual peripheral nerve stimulation thresholds as measured in mri gradient coils," *Journal of Magnetic Resonance Imaging*, vol. 17, no. 6, pp. 716–721, 2003.

[25] P. W. Goodwill, J. J. Konkle, B. Zheng, E. U. Saritas, and S. M. Conolly, "Projection x-space magnetic particle imaging," *IEEE transactions on medical imaging*, vol. 31, no. 5, pp. 1076–1085, 2012.

[26] J. J. Konkle, P. W. Goodwill, E. U. Saritas, B. Zheng, K. Lu, and S. M. Conolly, "Twenty-fold acceleration of 3d projection reconstruction mpi," *Biomedizinische Technik/Biomedical Engineering*, vol. 58, no. 6, pp. 565–576, 2013.

[27] J. Rahmer, B. Gleich, J. Weizenecker, A. Halkola, C. Bontus, J. Schmidt, I. Schmale, O. Woywode, T. Buzug, and J. Borgert, "Fast continuous motion of the field of view in magnetic particle imaging," in *Magnetic Particle Imaging (IWMPI), 2013 International Workshop on*, pp. 1–1, IEEE, 2013.

[28] P. W. Goodwill and S. M. Conolly, "Multidimensional x-space magnetic particle imaging," *IEEE transactions on medical imaging*, vol. 30, no. 9, pp. 1581–1590, 2011.

[29] B. J. Recoskie, T. J. Scholl, and B. A. Chronik, "The discrepancy between human peripheral nerve chronaxie times as measured using magnetic and electric field stimuli: the relevance to mri gradient coil safety," *Physics in medicine and biology*, vol. 54, no. 19, p. 5965, 2009.

[30] J. Reilly, "Magnetic field excitation of peripheral nerves and the heart: a comparison of thresholds," *Medical and Biological Engineering and Computing*, vol. 29, no. 6, pp. 571–579, 1991.

[31] M. I. Skolnik, *Introduction to Radar*, p. 52. Singapore: McGraw-Hill Book Company, 1962.

[32] O. B. Demirel, D. Sarica, and E. U. Saritas, "Rapid scanning in x-space mpi: Impacts on image quality," in *6th International Workshop on Magnetic Particle Imaging (IWMPI 2016): Book of Abstracts*, Infinite Science Publishing, 2016.

[33] J. Moreno-Aranda and A. Seireg, "Investigation of over-the-skin electrical stimulation parameters for different normal muscles and subjects," *Journal of Biomechanics*, vol. 14, no. 9, pp. 587–593, 1981.

[34] A. R. Ward, V. J. Robertson, and H. Ioannou, "The effect of duty cycle and frequency on muscle torque production using kilohertz frequency range alternating current," *Medical Engineering & Physics*, vol. 26, no. 7, pp. 569–579, 2004.

[35] R. E. Liebano, S. J. Waszczuk, and J. Corrêa, "The effect of burst-duty-cycle parameters of medium-frequency alternating current on maximum electrically induced torque of the quadriceps femoris, discomfort, and tolerated current amplitude in professional soccer players," *Journal of Orthopaedic & Sports Physical Therapy*, vol. 43, no. 12, pp. 920–926, 2013.

[36] N. Panagiotopoulos, R. L. Duschka, M. Ahlborg, G. Bringout, C. Debbeler, M. Graeser, C. Kaethner, K. Lüdtke-Buzug, H. Medimagh, J. Stelzner, T. M. Buzug, J. Barkhausen, F. M. Vogt, and J. Haegele, "Magnetic particle imaging: current developments and future directions," *International journal of nanomedicine*, vol. 10, p. 3097, 2015.

[37] W. T. Dixon, "Simple proton spectroscopic imaging.," *Radiology*, vol. 153, no. 1, pp. 189–194, 1984.

[38] M. A. Fischer, C. W. Pfirrmann, N. Espinosa, D. A. Raptis, and F. M. Buck, "Dixon-based mri for assessment of muscle-fat content in phantoms, healthy volunteers and patients with achillodynia: comparison to visual assessment of calf muscle quality," *European radiology*, vol. 24, no. 6, pp. 1366–1375, 2014.

[39] J. Canny, "A computational approach to edge detection," *IEEE Transactions on pattern analysis and machine intelligence*, no. 6, pp. 679–698, 1986.

[40] E. U. Saritas, P. W. Goodwill, G. Z. Zhang, and S. M. Conolly, "Magnetostimulation limits in magnetic particle imaging," *IEEE transactions on medical imaging*, vol. 32, no. 9, pp. 1600–1610, 2013.

[41] T. Knopp, S. Biederer, T. Sattel, J. Weizenecker, B. Gleich, J. Borgert, and T. Buzug, "Trajectory analysis for magnetic particle imaging," *Physics in medicine and biology*, vol. 54, no. 2, p. 385, 2008.

Appendix A

Multidimensional MPI Signal & Image Equation Derivations

$$G = \begin{bmatrix} -\alpha G_{zz} & G_{xy} & G_{xz} \\ G_{xy} & (\alpha - 1)G_{zz} & G_{yz} \\ G_{xz} & G_{yz} & G_{zz} \end{bmatrix} \tag{A.1}$$

The gradient matrix should be consistent with Maxwell equation's in source-free space. In other words, the sum of diagonal elements in G matrix should be zero. Formulation in 2.16 uses a cylindrically symmetric Maxwell z-gradient with zero off-diagonal elements and $\alpha = \frac{1}{2}$.

$$\begin{aligned} \dot{r} &= \frac{dr}{dt} \\ &= \frac{G\dot{x}_s(t)}{H_{sat}} \end{aligned} \tag{A.2}$$

$$
\begin{aligned}
\dot{\hat{r}} = \frac{d\hat{r}}{dt} &= \frac{d}{dt}(\frac{r}{\|r\|}) \\
&= \frac{1}{\|r\|}\left(\frac{dr}{dt}\right) + \left(\frac{d}{dt}\frac{1}{\|r\|}\right)r \\
&= \frac{\dot{r}}{\|r\|} + \left[\frac{d}{dt}\left(\frac{1}{\sqrt{r^T r}}\right)\right]r \\
&= \frac{\dot{r}}{\|r\|} + \left[-\frac{1}{2}(r^T r)^{3/2}\frac{d}{dt}(r^T r)\right]r \\
&= \frac{\dot{r}}{\|r\|} + \left[-\frac{1}{2(r^T r)^{3/2}}(\dot{r}^T r + r^T \dot{r})\right]r \\
&= \frac{\dot{r}}{\|r\|} + \frac{\dot{r}^T r}{\|r\|^3}r
\end{aligned}
\tag{A.3}
$$

$$
\frac{d}{dt}\mathcal{L}(\|r\|)\hat{r} = \frac{d}{dt}(\mathcal{L}(\|r\|))\hat{r} + \mathcal{L}(\|r\|)\dot{\hat{r}} \tag{A.4}
$$

If we solve the first part of Eq. A.4 we obtain following two formulas (Eq. A.5 represents tangential component of the derivative of the Langevin function and Eq. A.6 represents normal component of the derivative of the Langevin function):

$$
\begin{aligned}
\frac{d}{dt}\left(\mathcal{L}(\|r\|)\right)\hat{r} &= \dot{\mathcal{L}}(\|r\|)\frac{d}{dt}(\|r\|)\hat{r} \\
&= \dot{\mathcal{L}}(\|r\|)\frac{d}{dt}(\sqrt{r\cdot r})\hat{r} \\
&= \dot{\mathcal{L}}(\|r\|)\frac{1}{2}(r\cdot r)^{-1/2}(r\cdot\dot{r} + r\cdot\dot{r})\hat{r} \\
&= \dot{\mathcal{L}}(\|r\|)\frac{2r\cdot\dot{r}}{2\sqrt{r\cdot r}}\hat{r} \\
&= \dot{\mathcal{L}}(\|r\|)\frac{r\cdot\dot{r}}{\|r\|^2}r
\end{aligned}
\tag{A.5}
$$

$$\begin{aligned}\mathcal{L}(\|r\|)\dot{\hat{r}} &= \mathcal{L}(\|r\|)\left[\frac{\dot{r}}{\|r\|} - \frac{\dot{r}^T r}{\|r\|^3} r\right] \\ &= \frac{\mathcal{L}(\|r\|)}{\|r\|}\left[\dot{r} - \frac{\dot{r}^T r}{\|r\|^2} r\right] \\ &= \frac{\mathcal{L}(\|r\|)}{\|r\|}\left[\dot{r} - \frac{\dot{r}^T r}{\|r\|} \hat{r}\right] \\ &= \frac{\mathcal{L}(\|r\|)}{\|r\|}\left[\dot{r} - \frac{\dot{r} \cdot r}{\|r\|^2} r\right]\end{aligned} \tag{A.6}$$

Therefore, we can write the following equation for the derivative of the Langevin function:

$$\frac{d}{dt}\mathcal{L}(\|r\|)\hat{r} = \dot{\mathcal{L}}(\|r\|)\dot{r_{\|}} + \frac{\mathcal{L}(\|r\|)}{\|r\|}\dot{r_{\perp}} \tag{A.7}$$

$$\begin{aligned}s(t) &= \frac{d}{dt}\int\int\int B_1(u) m\rho(u)\mathcal{L}(\|r\|)\hat{r}du \\ &= \int\int\int B_1(u) m\rho(u)\left[\dot{\mathcal{L}}(\|r\|)\dot{r_{\|}} + \frac{\mathcal{L}(\|r\|)}{\|r\|}\dot{r}_{\perp}\right]du\end{aligned} \tag{A.8}$$

If we replace $r = \frac{G(x_s(t)-x)}{H_{sat}}$ in Eq. A.8, we can achieve the following:

$$\begin{aligned}s(t) = &\int\int\int B_1(u) m\rho(u)\dot{\mathcal{L}}\left(\frac{\|G(x_s(t)-u)\|}{H_{sat}}\right).\frac{\frac{G(x_s(t)-u)}{H_{sat}} \cdot \frac{G\dot{x}_s(t)}{H_{sat}}}{\frac{\|G(x_s(t)-u)\|^2}{H_{sat}}} G(x_s(t)-u)du \\ &+ \int\int\int B_1(u) m\rho(u)\frac{\mathcal{L}(\frac{\|G(x_s(t)-u)\|}{H_{sat}})}{\frac{\|G(x_s(t)-u)\|}{H_{sat}}}.\left[\frac{G\dot{x}_s(t)}{H_{sat}} - \left(\frac{\frac{G\dot{x}_s(t)}{H_{sat}} \cdot \frac{G(x_s(t)-u)}{H_{sat}}}{\frac{\|G(x_s(t)-u)\|^2}{H_{sat}}}\right)\frac{G(x_s(t)-u)}{H_{sat}}\right]\end{aligned} \tag{A.9}$$

We can simplify Eq. A.9 bu using $a \cdot b = ab^T$ and also $x = x_s(t)$:

$$
\begin{aligned}
s(t) = &\int\int\int B_1(u) m\rho(u) \dot{\mathcal{L}}\left[\frac{\|Gx\|}{H_{sat}}\right] . \frac{[\frac{G\dot{x}_s(t)}{H_{sat}}]^T [Gx]}{\|Gx\|^2}[Gx]\Bigg|_{x=x_s(t)} \\
&+ \int\int\int B_1(u) m\rho(u) \frac{\mathcal{L}(\frac{\|Gx\|}{H_{sat}})}{\frac{\|Gx\|}{H_{sat}}} . \left[\frac{G\dot{x}_s(t)}{H_{sat}} - \frac{[\frac{G\dot{x}_s(t)}{H_{sat}}]^T [Gx]}{\|Gx\|^2}[Gx]\right]\Bigg|_{x=x_s(t)}
\end{aligned} \tag{A.10}
$$

By using $(a \cdot b)b = bb^T a$ equality to obtain a simple version of PSF, we can write the multi-dimensional MPI signal equation as follows:

$$
s(t) = B_1(x) m\rho(x) * * * \frac{\|\dot{x}_s\|}{H_{sat}} h(x) \hat{\dot{x}}_s \Bigg|_{x=x_s(t)} \tag{A.11}
$$

where $h(x)$ represents the PSF by using the following steps:

$$
a = G \tag{A.12}
$$

$$
b = \frac{Gx}{\|Gx\|} \tag{A.13}
$$

$$
\begin{aligned}
\dot{\mathcal{L}}(\frac{\|Gx\|}{H_{sat}}) \left[\frac{\frac{G\dot{x}_s(t)}{H_{sat}}}{\|Gx\|^2} \cdot Gx\right] Gx &= \dot{\mathcal{L}}\left(\frac{\|Gx\|}{H_{sat}}\right) \frac{\dot{x}_s(t)}{H_{sat}} [a \cdot b] b \\
&= \dot{\mathcal{L}}\left(\frac{\|Gx\|}{H_{sat}}\right) \frac{\dot{x}_s(t)}{H_{sat}} bb^T a \\
&= \dot{\mathcal{L}}\left(\frac{\|Gx\|}{H_{sat}}\right) \frac{\|\dot{x}_s(t)\|}{H_{sat}} \hat{\dot{x}}_s \frac{Gx}{\|Gx\|} \left[\frac{Gx}{\|Gx\|}\right]^T G
\end{aligned} \tag{A.14}
$$

$$\begin{aligned}
\frac{\mathcal{L}(\frac{\|Gx\|}{H_{sat}})}{\frac{\|Gx\|}{H_{sat}}}\left[\frac{G\dot{x}_s(t)}{H_{sat}} - \frac{G\dot{x}_s(t)\cdot Gx}{\|Gx\|^2}Gx\right] &= \frac{\mathcal{L}(\frac{\|Gx\|}{H_{sat}})}{\frac{\|Gx\|}{H_{sat}}}\left[\frac{a\dot{x}_s(t)}{H_{sat}} - (a\dot{x}_s(t)\cdot b)b\right] \\
&= \frac{\mathcal{L}(\frac{\|Gx\|}{H_{sat}})}{\frac{\|Gx\|}{H_{sat}}}\frac{\dot{x}_s(t)}{H_{sat}}\left[a - (a\cdot b)b\right] \\
&= \frac{\mathcal{L}(\frac{\|Gx\|}{H_{sat}})}{\frac{\|Gx\|}{H_{sat}}}\frac{\|\dot{x}_s\|}{H_{sat}}\hat{\dot{x}}_s\left[a - bb^T a\right] \\
&= \frac{\mathcal{L}(\frac{\|Gx\|}{H_{sat}})}{\frac{\|Gx\|}{H_{sat}}}\frac{\|\dot{x}_s\|}{H_{sat}}\hat{\dot{x}}_s\left[I - \frac{Gx}{\|Gx\|}\left[\frac{Gx}{\|Gx\|}\right]^T\right]G
\end{aligned} \tag{A.15}$$

And we have the PFS as h(x) as follows:

$$h(x) = \dot{\mathcal{L}}\left(\frac{\|Gx\|}{H_{sat}}\right)\frac{Gx}{\|Gx\|}\left[\frac{Gx}{\|Gx\|}\right]^T G + \frac{\mathcal{L}\left(\frac{\|Gx\|}{H_{sat}}\right)}{\frac{\|Gx\|}{H_{sat}}}\left(I - \frac{Gx}{\|Gx\|}\left[\frac{Gx}{\|Gx\|}\right]^T\right)G \tag{A.16}$$

Assuming we have $\hat{e}_1 = \begin{bmatrix} 0 & 0 & 1 \end{bmatrix}^T$ as the excitation vector along z-axis and $G = \begin{bmatrix} G_{xx} & 0 & 0 \\ 0 & G_{yy} & 0 \\ 0 & 0 & G_{zz} \end{bmatrix}$ and using $h_1(x) = \dot{\mathcal{L}}\left(\frac{\|Gx\|}{H_{sat}}\right)\frac{Gx}{\|Gx\|}\left[\frac{Gx}{\|Gx\|}\right]^T G$ and $h_2(x) = \frac{\mathcal{L}\left(\frac{\|Gx\|}{H_{sat}}\right)}{\frac{\|Gx\|}{H_{sat}}}\left(I - \frac{Gx}{\|Gx\|}\left[\frac{Gx}{\|Gx\|}\right]^T\right)G$ we can write the following for collinear part of PSF:

$$h_{\|}(x) = \hat{e_1}\cdot h_1(x)\hat{e}_1 + \hat{e}_1 \cdot h_2(x)\hat{e}_1 \tag{A.17}$$

and define the following for simplicity:

$$\|Gx\| = \sqrt{(Gx)^T Gx} = \sqrt{(G_{xx}x)^2 + (G_{yy}y)^2 + (G_{zz}z)^2} = H(x,y,z) \tag{A.18}$$

We can solve the collinear PSF by dividing it into 2 parts for simplicity. The first part is $\hat{e}_1 \cdot h_1(x)\hat{e}_1$ and the second part is $\hat{e}_1 \cdot h_2(x)\hat{e}_1$. For the 1st part:

$$\hat{e}_1 \cdot h_1(x)\hat{e}_1 = \begin{bmatrix} 0 \\ 0 \\ 1 \end{bmatrix} \cdot \left[\dot{\mathcal{L}}\left(\frac{H(x,y,z)}{H_{sat}} \right) \frac{\begin{bmatrix} G_{xx} & 0 & 0 \\ 0 & G_{yy} & 0 \\ 0 & 0 & G_{zz} \end{bmatrix} \begin{bmatrix} x \\ y \\ z \end{bmatrix}}{H(x,y,z)} \times \right.$$
$$\left. \frac{\left(\begin{bmatrix} G_{xx} & 0 & 0 \\ 0 & G_{yy} & 0 \\ 0 & 0 & G_{zz} \end{bmatrix} \begin{bmatrix} x \\ y \\ z \end{bmatrix} \right)^T}{H(x,y,z)} \begin{bmatrix} G_{xx} & 0 & 0 \\ 0 & G_{yy} & 0 \\ 0 & 0 & G_{zz} \end{bmatrix} \right] \begin{bmatrix} 0 \\ 0 \\ 1 \end{bmatrix}$$

$$\begin{aligned} \hat{e}_1 \cdot h_1(x)\hat{e}_1 &= \begin{bmatrix} 0 \\ 0 \\ 1 \end{bmatrix} \cdot \left[\frac{\dot{\mathcal{L}}\left(\frac{H(x,y,z)}{H_{sat}} \right)}{H(x,y,z)^2} \begin{bmatrix} G_{xx} G_{zz}^2 xz \\ G_{yy} G_{zz}^2 yz \\ G_{zz}^3 z^2 \end{bmatrix} \right] \\ &= \frac{\dot{\mathcal{L}}\left(\frac{H(x,y,z)}{H_{sat}} \right)}{H(x,y,z)^2} G_{zz}^3 z^2 \end{aligned} \tag{A.19}$$

For the 2nd part:

$$\hat{e}_1 \cdot h_2(x)\hat{e}_1 = \begin{bmatrix} 0 \\ 0 \\ 1 \end{bmatrix} \cdot \left[\frac{\mathcal{L}\left(\frac{H(x,y,z)}{H_{sat}}\right)}{\frac{\|Gx\|}{H_{sat}}} \left(I - \frac{\begin{bmatrix} G_{xx} & 0 & 0 \\ 0 & G_{yy} & 0 \\ 0 & 0 & G_{zz} \end{bmatrix} \begin{bmatrix} x \\ y \\ z \end{bmatrix}}{H(x,y,z)} \times \right.$$
$$\left. \frac{\left(\begin{bmatrix} G_{xx} & 0 & 0 \\ 0 & G_{yy} & 0 \\ 0 & 0 & G_{zz} \end{bmatrix} \begin{bmatrix} x \\ y \\ z \end{bmatrix} \right)^T}{H(x,y,z)} \right) \begin{bmatrix} G_{xx} & 0 & 0 \\ 0 & G_{yy} & 0 \\ 0 & 0 & G_{zz} \end{bmatrix} \Bigg] \begin{bmatrix} 0 \\ 0 \\ 1 \end{bmatrix}$$

$$\begin{aligned} \hat{e}_1 \cdot h_2(x)\hat{e}_1 &= \frac{\mathcal{L}\left(\frac{H(x,y,z)}{H_{sat}}\right)}{\frac{H(x,y,z)}{H_{sat}}} \begin{bmatrix} 0 \\ 0 \\ 1 \end{bmatrix} \cdot \left[\begin{bmatrix} 0 \\ 0 \\ G_{zz} \end{bmatrix} - \frac{\begin{bmatrix} G_{xx}G_{zz}^2 xz \\ G_{yy}G_{zz}^2 yz \\ G_{zz}^3 z^2 \end{bmatrix}}{H(x,y,z)^2} \right] \\ &= \frac{\mathcal{L}\left(\frac{H(x,y,z)}{H_{sat}}\right)}{\frac{H(x,y,z)}{H_{sat}}} G_{zz} \left(1 - \frac{G_{zz}^2 z^2}{H(x,y,z)^2} \right) \end{aligned} \tag{A.20}$$

At the end, we have the collinear PSF as follows:

$$h_{\|}(x,y,z) = \frac{\dot{\mathcal{L}}\left(\frac{H(x,y,z)}{H_{sat}}\right)}{H(x,y,z)^2} G_{zz}^3 z^2 + \frac{\mathcal{L}\left(\frac{H(x,y,z)}{H_{sat}}\right)}{\frac{H(x,y,z)}{H_{sat}}} G_{zz} \left(1 - \frac{G_{zz}^2 z^2}{H(x,y,z)^2} \right) \tag{A.21}$$

If we follow the same operations for the transverse PSF by using $\dot{e}_2 = \begin{bmatrix} 1 & 0 & 0 \end{bmatrix}^T$ and $h_{\perp,1}(x) = \dot{e}_2 \cdot h_1(x)\hat{e}_1 + \dot{e}_2 \cdot h_2(x)\hat{e}_1$ by using same $h(x)$ as before and assigning first parts as $\dot{e}_2 \cdot h_1(x)\hat{e}_1$ and second part as $\dot{e}_2 \cdot h_2(x)\hat{e}_1$, we find the following:

$$\begin{aligned}\dot{e}_2 \cdot h_1(x)\hat{e}_1 &= \frac{\dot{\mathcal{L}}\left[\frac{H(x,y,z)}{H_{sat}}\right]}{H(x,y,z)^2}\left[\begin{bmatrix}1\\0\\0\end{bmatrix}\cdot\begin{bmatrix}G_{xx}G_{zz}^2xz\\G_{yy}G_{zz}^2yz\\G_{zz}^3z^2\end{bmatrix}\right] \\ &= \frac{\dot{\mathcal{L}}\left[\frac{H(x,y,z)}{H_{sat}}\right]}{H(x,y,z)^2}G_{xx}G_{zz}^2xz\end{aligned} \tag{A.22}$$

For the second part:

$$\begin{aligned}\dot{e}_2 \cdot h_2(x)\hat{e}_1 &= \frac{\mathcal{L}\frac{H(x,y,z)}{H_{sat}}}{\frac{H(x,y,z)}{H_{sat}}}\left[\begin{bmatrix}1\\0\\0\end{bmatrix}\cdot\begin{bmatrix}0\\0\\G_{zz}\end{bmatrix} - \frac{\begin{bmatrix}1\\0\\0\end{bmatrix}\cdot\begin{bmatrix}G_{xx}G_{zz}^2xz\\G_{yy}G_{zz}^2yz\\G_{zz}^3z^2\end{bmatrix}}{H(x,y,z)^2}\right] \\ &= \frac{\mathcal{L}\frac{H(x,y,z)}{H_{sat}}}{\frac{H(x,y,z)}{H_{sat}}}\frac{G_{xx}G_{zz}^2xz}{H(x,y,z)^2}\end{aligned} \tag{A.23}$$

Then, we obtain the transverse PSF as follow:

$$h_{\perp,1}(x,y,z) = \frac{\dot{\mathcal{L}}\left[\frac{H(x,y,z)}{H_{sat}}\right]}{H(x,y,z)^2}G_{xx}G_{zz}^2xz + \frac{\mathcal{L}\frac{H(x,y,z)}{H_{sat}}}{\frac{H(x,y,z)}{H_{sat}}}\frac{G_{xx}G_{zz}^2xz}{H(x,y,z)^2} \tag{A.24}$$

Appendix B

Custom MPI Simulation Toolbox

For the work in Chapter 5 of this thesis, I developed a custom MPI simulation toolbox in MATLAB environment. It has a variety of features for testing different scanning trajectories along with different scanning parameters. It has four essential parts: (1) PSF formation and image convolution, (2) trajectory selection, (3) scanning parameters and (4) image reconstruction. These features are shown with the GUI of MPI simulation toolbox in Fig. B.1.

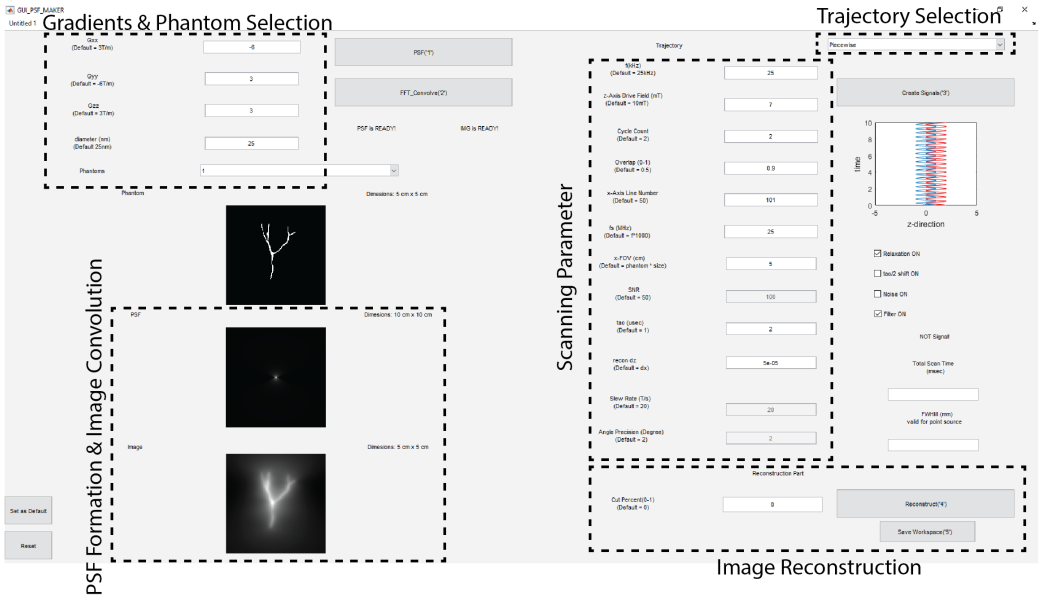

Figure B.1: A screen-shot from the MPI Simulation Toolbox

In the first part of the toolbox, one can choose different gradients to create the corresponding PSFs. After the creation of the PSF, MPI image can be formed by the convolution of phantom and PSF. Fig. B.2 shows some example PSFs with corresponding convolved images.

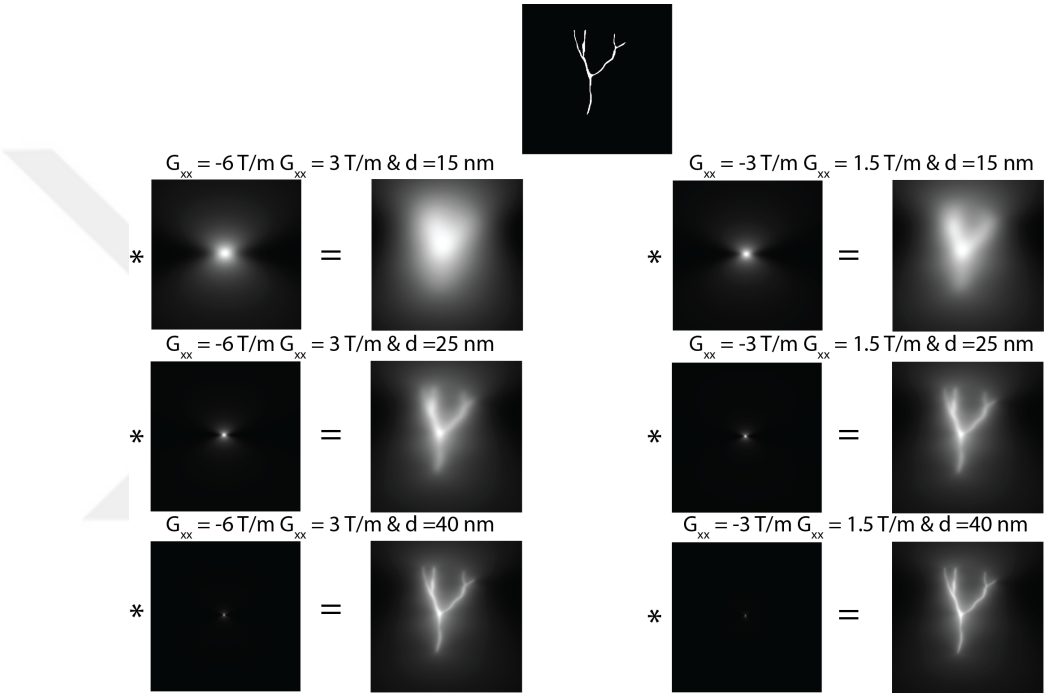

Figure B.2: Phantom #1 with different SPIO diameter and gradients

In the second part, one can choose 3 different trajectories , as shown in Fig. B.3.

In the third part, one can use the following parameters corresponding with the different trajectories.

1. Drive Field Frequency $[kHz]$ (Default Value: 25)
2. Drive Field Amplitude $[mT]$ (Default Value: 10, Default Direction: z-axis)
3. Cycle Count (Default Value: 2)
4. Overlap (Default Value: 0.5)
5. Line Number (Default Value: 50, Default Direction: x-axis)

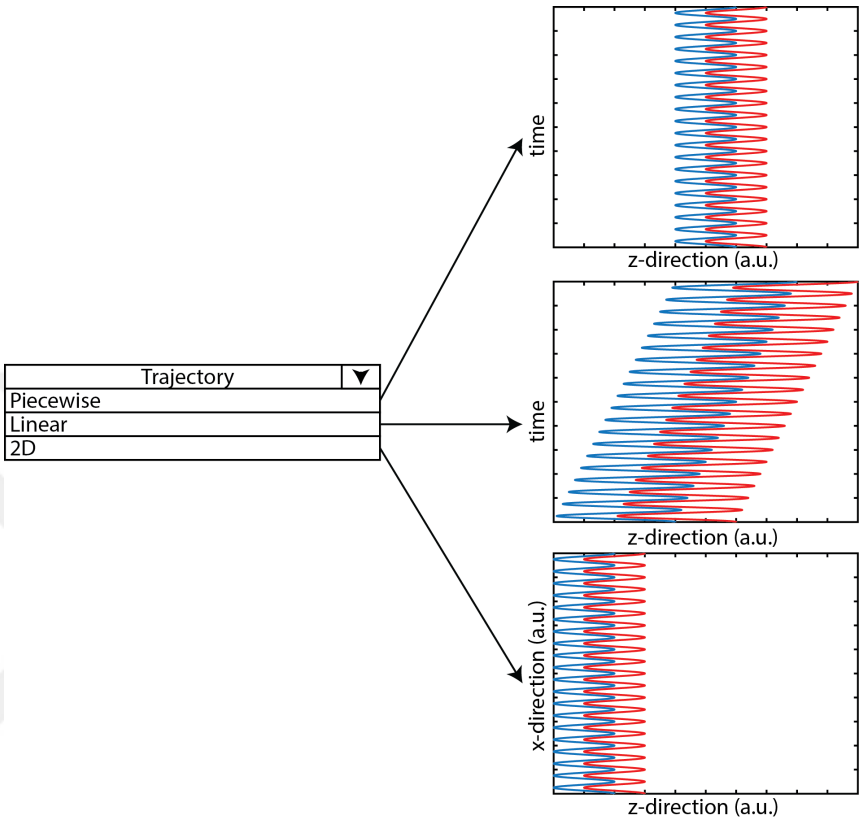

Figure B.3: Different Trajectories

6. Sampling Frequency $[MHz]$ (Default Value: Drive Field Frequency * 1000)
7. FOV $[cm]$ (Default Value: Phantom X-axis coverage)
8. SNR (Default Value: 50)
9. Relaxation Time Constant τ $[\mu s]$ (Default Value: 2)
10. Reconstruction Pixel Size $[m]$ (Default Value: Phantom Pixel Size)
11. Slew Rate $[T/s]$ (Default Value: 20)
12. Angle Precision $[^o]$ (Default Value: 2)

In the final part (image reconstruction), x-space image reconstruction with DC recovery is used to form images [8].